Energy 294 (2024) 130251

Contents lists available at ScienceDirect

Energy

journal homepage: www.elsevier.com/locate/energy

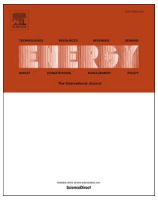

Development of a comprehensive method to estimate the optical, thermal and electrical performance of a complex PV window for building integration

Xue Li [a,**], Yanyi Sun [a,b], Xiao Liu [a], Yang Ming [a], Yupeng Wu [a,*]

[a] Department of Architecture and Built Environment, Faculty of Engineering, The University of Nottingham, University Park, Nottingham, NG7 2RD, United Kingdom
[b] Department of Civil Engineering, Surveying and Construction Management, School of Built Environment and Geography, Faculty of Engineering, Computing and the Environment, Kingston University, United Kingdom

A R T I C L E I N F O

Handling Editor: Prof X Ou

Keywords:
Building integrated PV
Complex PV window
Solar heat gain coefficient
Power output
CFD
Ray-tracing

A B S T R A C T

Increasing concerns over energy consumption and greenhouse gas emissions in buildings have contributed to the emerging of innovative PV glazing technologies to improve the building energy performance. However, some of these glazing systems have complex structures, making it challenging to investigate their optical, thermal and electrical performance for estimating their energy saving potential in buildings. In this research, a validated Computational Fluid Dynamics (CFD) combined with a ray-tracing model has been developed to accurately predict the optical, thermal and electrical performance of complex PV glazing systems under varying incident angles. A ray-tracing model is developed to calculate the light transmittance of the window and the solar energy absorbed by each solid element and PV cells. To estimate temperature profiles (e.g., PV temperature and window temperature) and secondary heat within the window, the results from the ray-tracing analysis, which detail the solar flux absorbed by each layer, are inputted into a validated CFD model as boundary conditions. Using the CFD combined ray-tracing calculation illustrated above, the Solar Heat Gain Coefficient (SHGC) of these complex PV window systems can be obtained. Furthermore, a PV modelling algorithm is developed to predict the power output based on the simulated PV temperature. This procedure is implemented to investigate a Crossed Compound Parabolic Concentrator Photovoltaic (CCPC-PV) window, which serves as an example of a complex PV glazing system in this study. The developed optical, thermal and electrical models have been validated through experimental tests. Additionally, new configurations have been designed to explore the impact of the pitch between adjacent optics on the SHGC and power output of the window. The results show that the original window (1.77 mm-pitch) possesses the maximum PV temperature of 64.73 °C and the maximum window inside surface temperature of 61.58 °C under National Fenestration Rating Council (NFRC) standard. Meanwhile the PV efficiency is 15.21 % and the SHGC is 0.463. The SHGC value of this innovative PV window is notably lower than that of a conventional double-glazed window, which has a SHGC value of 0.813. This reduction in SHGC decreases the likelihood of overheating issues, especially during the summer months.

1. Introduction

In building energy and daylight simulations, glass windows are typically characterised by three key metrics: U-value, Solar Heat Gain Coefficient (SHGC) and Visible Transmittance (VT) [1–4]. The U-value of a building window is used to indicate the heat loss/gain through it due to indoor and outdoor environmental temperature difference [5]. Therefore, it reflects a window's thermal insulation property, with lower values being preferable for energy efficiency [6]. The Visible Transmittance (VT) represents the portion of visible light that passes through a glazing system, which is crucial for indoor daylight [2,5]. Windows often have high U-values, making them the thermal weakest part compared to other building envelope components [7,8]. Additionally, windows can be sources of overheating and glare issues in buildngs [9]. To address these concerns associated with traditional window systems, innovative glazing technologies have been widely developed and investigated in recent decades [10]. For example, Sun et al. [11]

---

[*] Corresponding author.
[**] Corresponding author.
E-mail addresses: Xue.Li@nottingham.ac.uk (X. Li), Yupeng.Wu@nottingham.ac.uk (Y. Wu).

https://doi.org/10.1016/j.energy.2024.130251
Received 3 October 2023; Received in revised form 7 December 2023; Accepted 2 January 2024

Nomenclature

Symbols

α	absorptance
τ	transmittance
θ	solar incident angle
φ	solar azimuth angle
λ	wavelength nm

also, thermal conductivity of air W/m·K

η	efficiency
δ	temperature coefficient/°C
c_p	specific heat capacity J/(kg·K)
A	area m^2
C	concentration ratio
D	distance M
h	thermal conductance $W/m^2 \cdot K$
I	current A
N	fraction of external solar radiation that absorbed by the window then released inward -
P	electrical power W
Q	heat flux W
q	heat flux per unit area W/m^2
S	volume heat source W/m^3
T	air temperature °C
t	pv temperature °C

Subscripts

a	air
e	electric

also, exterior

i	interior
g	glass

also, geometry

h	heat
in	incident
t	transmitted
r	reflected
op	optical
pv	photovoltaic
sc	short current
st	standard
x, y	cartesian coordinates

Dimensionless numbers

Pr	Prandtl number
Gr	Grashof number

Abbreviation

AM	air mass
BSDFs	bidirectional scattering distribution functions
CPV	concentrating photovoltaic
CCPC	crossed compound parabolic concentrator
CCPC-PV	crossed compound parabolic concentrator photovoltaic
CFD	computational fluid dynamics
PS-TIM	parallel slat transparent insulation material
STPV	semi-transparent photovoltaic
SHGC	solar heat gain coefficient
VT	visible transmittance
S2S	surface to surface
WWR	window to wall ratio

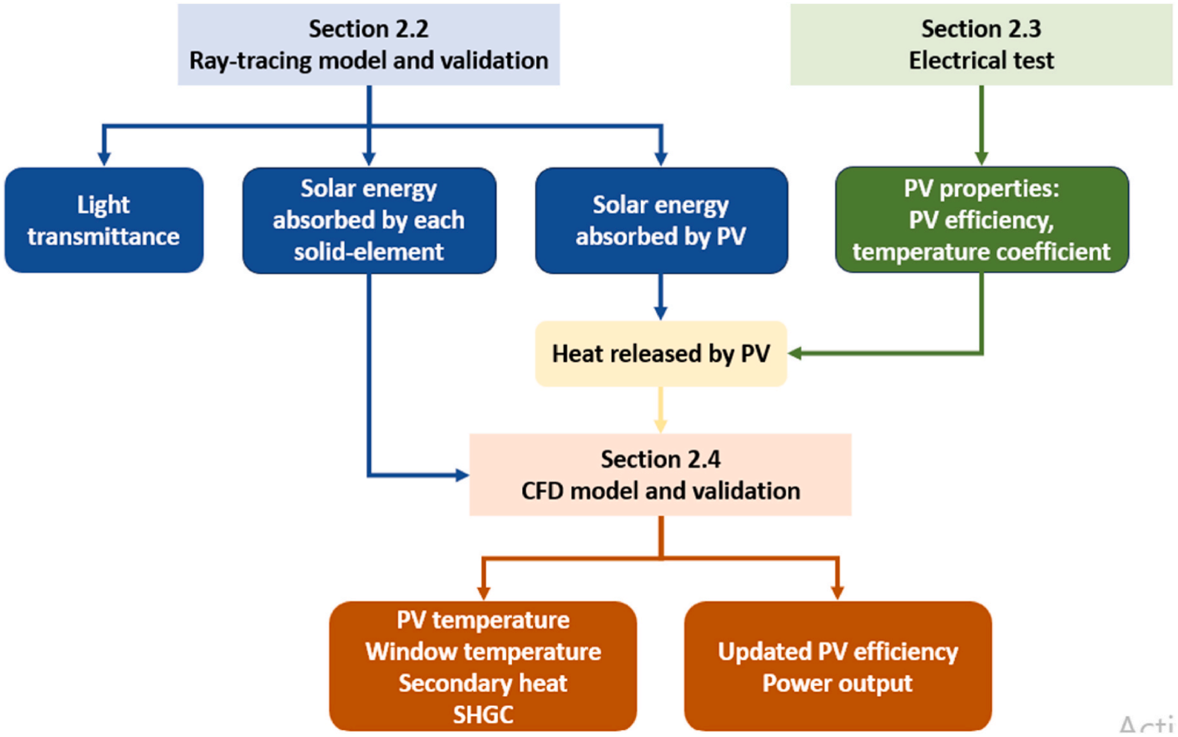

Fig. 1. CFD combined ray-tracing method to predict the optical, thermal and electrical performance of the CCPC-PV window.

Table 1
Boundary conditions for CFD combined ray-tracing simulations.

Standards	NFRC 200
Indoor air temperature	24 °C
Inside surface heat transfer coefficient	7.7 W/m^2 •K
Outdoor air temperature	32 °C
Outside surface heat transfer coefficient	25 W/m^2 •K
Outdoor solar radiation	783 W/m^2

investigated the thermal (U-value) and optical (VT) performance of a double-glazed window with Parallel Slat Transparent Insulation Material (PS-TIM). A two-dimensional CFD model was developed to explore the heat transfer into the double-glazed air cavity, both with and without PS-TIM. Additionally, a ray-tracing model was used to analyse the optical transmittance of the systems under different solar incidence angles. The results showed that incorporating a PS-TIM structure between the glass panes can reduce thermal conductance by 35%–46 % while maintaining high light transmittance. In addition, they also conducted an investigation into the daylight performance of the double-glazed window with PS-TIM, using RADIANCE in combination with Bidirectional Scattering Distribution Functions (BSDFs). The results showed that it achieves a homogeneous distribution of daylight within the internal working space and effectively reduces glare [12].

The SHGC represents a crucial indicator of window properties that influences the thermal and energy performance of buildings [13]. However, there is a limited body of literature dedicated to estimating it for innovative window designs [14]. This scarcity of studies can be attributed to the complexity and challenges associated with calculating SHGC, especially for windows with complex structures and PV cells. The SHGC is defined as the fraction of external solar radiation that is admitted through a window, both directly transmitted, and absorbed by the window then subsequently conducted, convected, and radiated to the interior of the building (secondary heat) [15–17]. This definition can be expressed as Eq. (1) [18]. Where τ (transmittance) and α (absorptance) are optical properties of layers and N is the fraction of the solar energy absorbed by window layers flowing inwards. Optical properties

Table 2
Independent test results of the light source for the ray-tracing simulation.

The number of rays	Total solar radiation incident on window outside surface (W/m^2)		
	0° incident angle	30° incident angle	60° incident angle
29701	1000.3	864.54	501.13
119401	999.72	865.92	499.80
269101	999.12	865.17	499.57
478801	999.79	865.74	499.95
748501	999.49	865.56	499.61
1078201	999.37	865.64	499.30

Table 3
Optical properties of the materials used in the ray-tracing model [11,46].

Material properties	Float glass	Sylgard 184	Topas (Polyolefin/Zeonex: COC Polymer)
Refraction index	1.52	1.42	1.53
Absorption coefficient (/mm)	0.01	0.01	0.002

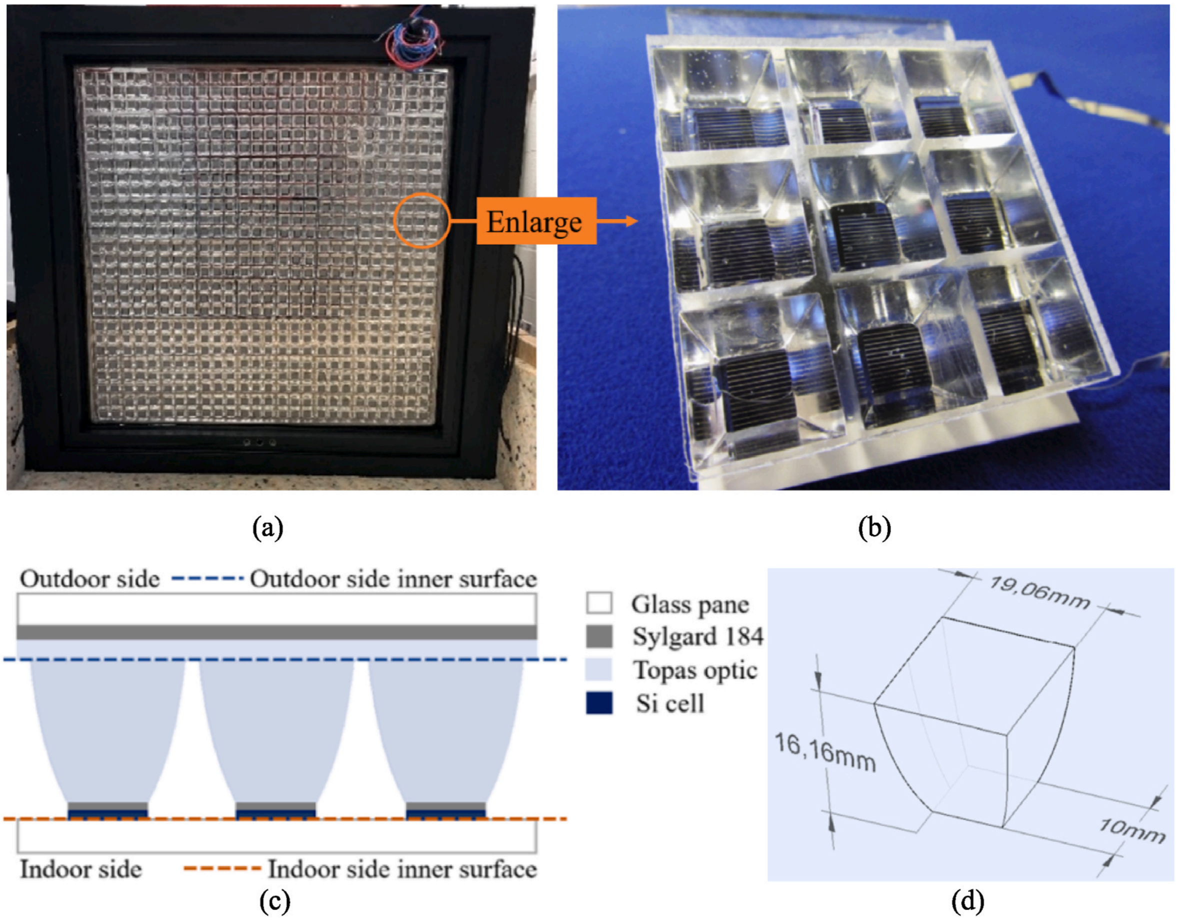

Fig. 2. Pictures of the (a) CCPC-PV window, (b) 3 × 3 CCPC-PV unit, (c) cross sectional view of the CCPC-PV window with detailed configuration, and (d) schematic sketch of a single CCPC optic.

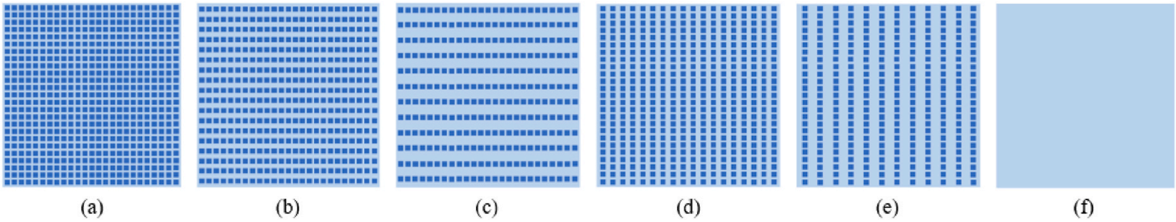

Fig. 3. Different configurations. For left three models, $D_x = 5$ mm & $D_y =$ (a) 5 mm, (b) 15 mm and (c) 30 mm; for right three models, $D_y = 5$ mm & $D_x =$ (d) 15 mm, (e) 30 mm, and (f) reference double-glazed window.

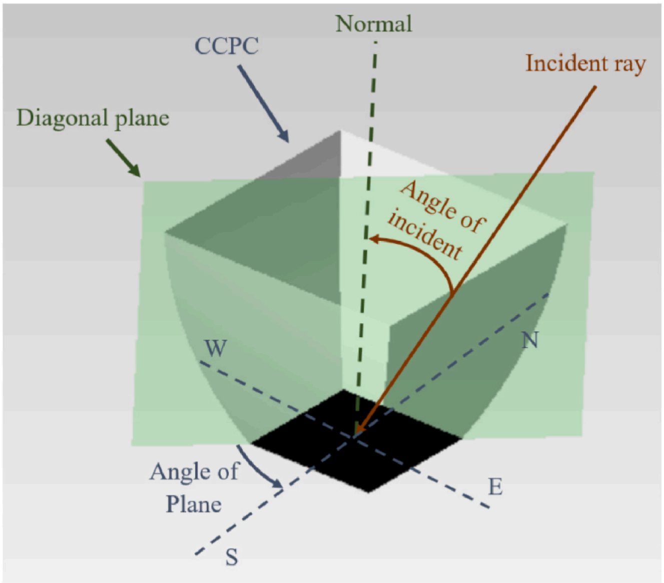

Fig. 4. Incident angle and plane angle of the CCPC optic.

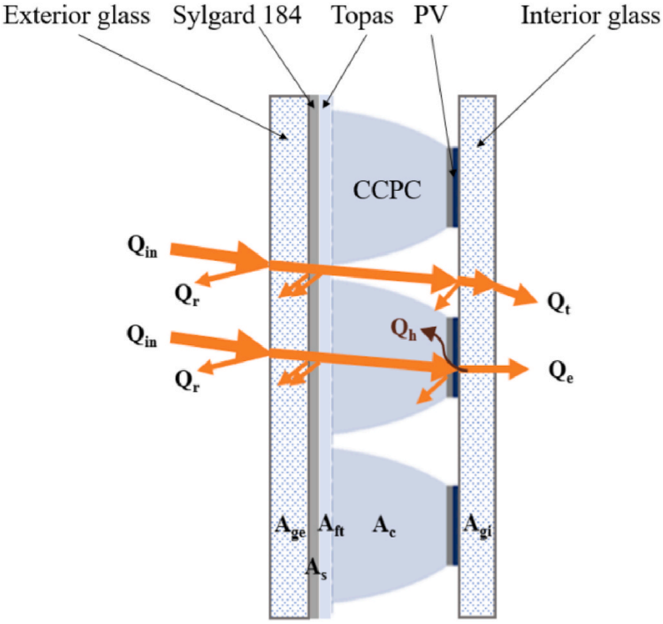

Fig. 5. Light flow through the CCPC-PV window.

are all angle (θ) and wavelength (λ) dependent. The SHGC of a window depends not only on the material properties, such as the light transmittance and absorptance, but also the indoor and outdoor environmental conditions, such as air temperature and wind speed [19,20]. Typical SHGC values for building windows range from 0.2 to 0.7 [5]. The lower a window's SHCG, the less solar heat it transmits [21], and vice versa. A higher SHGC is important for reducing heating loads in winter but can lead to overheating issues in summer [22]. Therefore, determining the SHGC value of a glazing system is critical for predicting its effects on the annual energy performance of a building fitted with such a glazing system [23,24].

$$SHGC = \tau(\theta, \lambda) + N \times \alpha(\theta, \lambda) \tag{1}$$

Various mathematical models have been developed to simulate the SHGC of different kinds of window glazing systems, such as the traditional double-glazed system [25,26] and PV glazing system [27]. Standard calculation procedures for SHGC simulation, such as ISO 15099 [25], are available for simpler glazing systems like multi-pane glazing. Window simulation tools, such as Window 7, have been developed with the capability to model the SHGC of complex glazing systems, including venetian blinds, roller shades, cellular shades, fritted glazing, solar screens, and chromogenic glazing, etc., at different incident angles [28]. However, for some complex glazing systems attached to intricate structures (e.g., solar optics) and PV cells, which cannot be simulated by existing models or lack detailed information (e.g., geometry and material properties) for simulation, the experimental method is often employed. There are two calorimetric methods used for SHGC measurement: indoor calorimeter with solar simulator [17,29–31] and outdoor calorimeters with or without sun tracking capability [32,33]. Using the indoor calorimeter method, Chen [29] measured the SHGC of a selected thin-film Semi-Transparent PV (STPV) glazing using SERIS' indoor calorimetric hot box and solar simulator. Calibrations for the spectrum, irradiance uniformity and temporal stability of the solar simulator were conducted before the actual test. The results showed that when the STPV specimen was connected to a load, the SHGC value was reduced by around 0.01–0.03. In the case of the outdoor calorimeter, Hans et al. [32] measured the SHGC of a glazing with venetian blind shading system and the measurement results were also verified using the numerical modelling.

The advantage of the experimental measurement is that the measured sample is treated as a 'black box' . In other words, the structure of the window glazing is not restricted, whether it is a simple traditional system or those with complex optics and PV cells. However, the complicated procedure, time-consuming test as well as the high expense limits its wide use. Recently, the combination of Computational Fluid Dynamics (CFD) and ray-tracing methods to calculate the temperature field and heat loss through various solar systems has been widely used in research [34–40]. The ray-tracing technique can be used to simulate the detailed light behaviours within the system featuring complex structures and to calculate optical properties, such as the light transmittance and absorption. Then the absorbed solar energy can be input into CFD as one of boundary conditions to simulate the temperature filed and heat flow through the system. For example, Craig [34,35] investigated the heat loss from a tubular cavity receiver, which can absorb the concentrated solar energy from a parabolic dish at various inclination angles and wind speeds. The solar energy distributed into the receiver was modeled using the ray-tracing software, SolTrace. And then

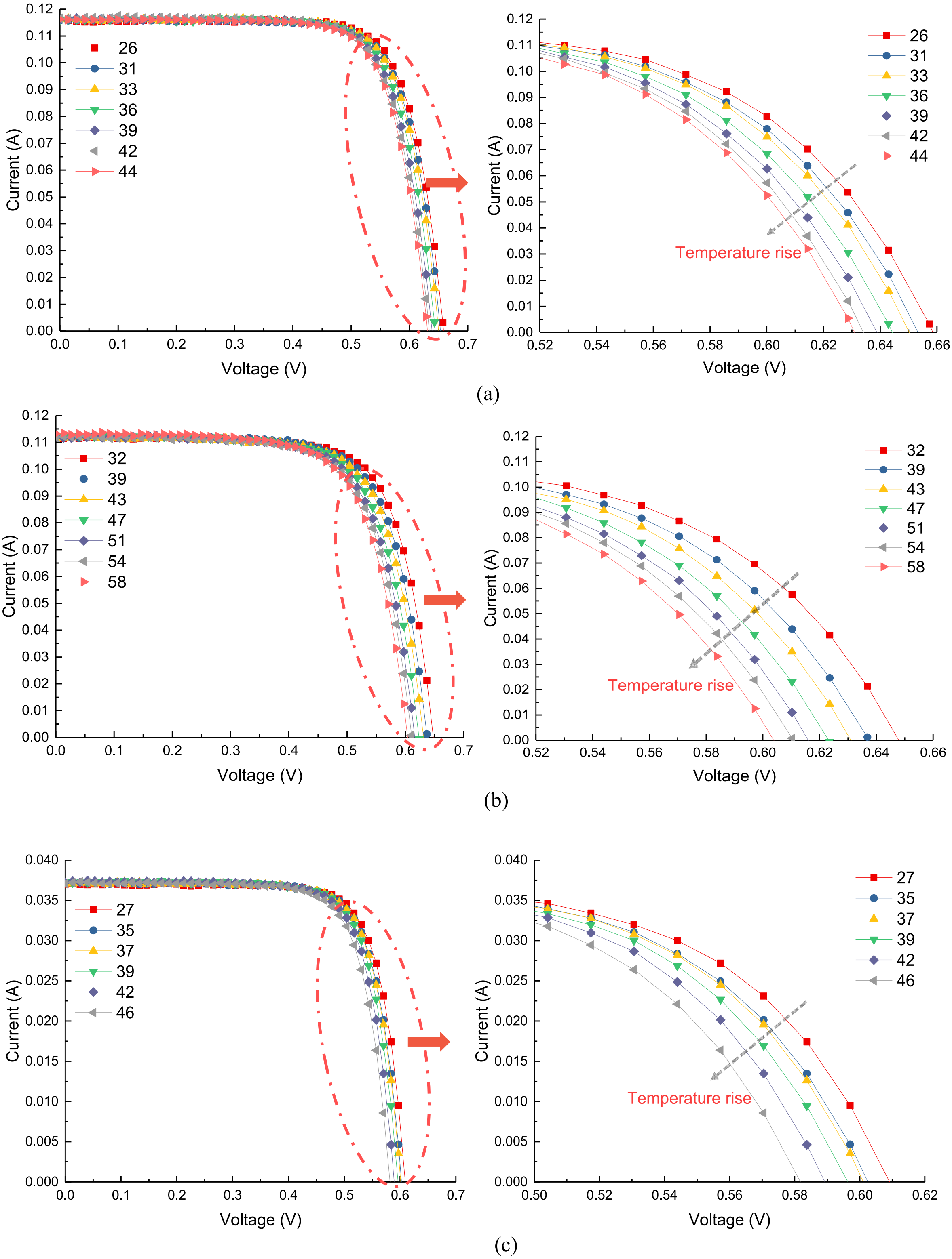

(a)

(b)

(c)

Fig. 6. I–V curve at 1000 W/m^2 solar radiation with different cell temperatures for (a) glass CPV, (b) topas CPV and (c) PV with no concentrator.

it was transformed as a volumetric source and input into a heat transfer model in CFD. The heat transfer model was validated by an experimental heating test using a blower and burner at its inlet. Ultimately, heat losses due to the thermal radiation out of the cavity, natural convection and forced convection were presented.

The CFD combined ray-tracing method has also garnered attention from researchers investigating window glazing systems. For example, Demanega et al. [41] investigated the temperature field and SHGC value of a complex fenestration system (a triple-glazed window, composed by two sealed cavities and curved commercial blinds on the exterior side) using CFD combined ray-tracing method, which shows the feasibility of using this method to calculate the SHGC of the glazing system with complex structures. However, the SHGC is more complicated for window glazing system containing solar optics and PV cells, such as the

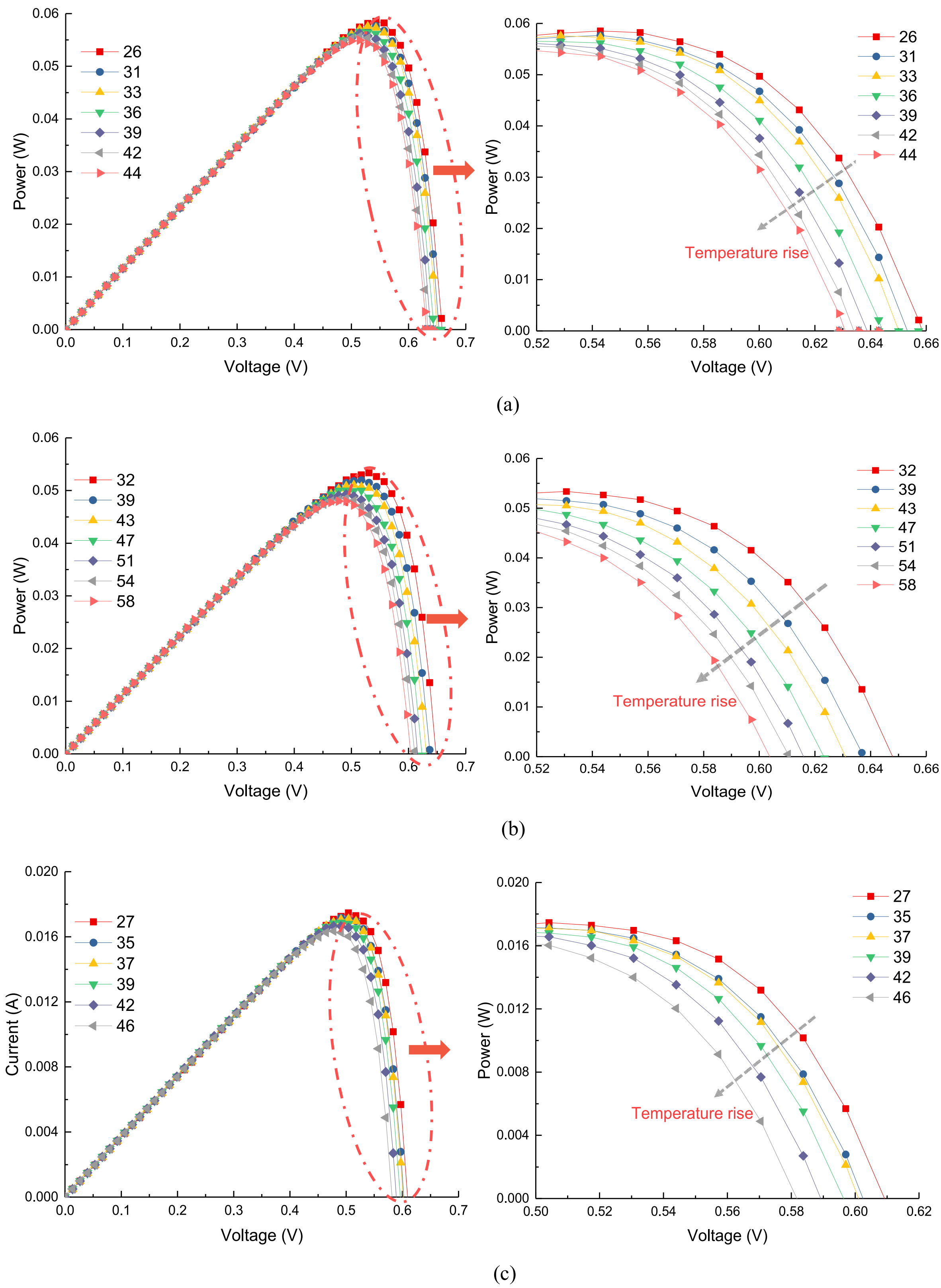

Fig. 7. P–V curve at 1000 W/m^2 solar radiation with different cell temperatures for (a) glass CPV, (b) topas CPV and (c) PV with no concentrator.

Crossed Compound Parabolic Concentrator Photovoltaic (CCPC-PV) Window. This is because the heat dissipation from PV power generation also participates in the window heat transfer and those inward to the indoor space should be included in the SHGC calculation as shown in Eq. (2). The amount of heat released by PV power generation is affected by both of the optical efficiency (η_{op}) and PV conversion efficiency (η_{pv}). The optical efficiency (η_{op}) of the CCPC-PV window is highly angle-dependent, while the PV conversion efficiency (η_{pv}) is temperature-dependent especially for those attached to concentrators (PV temperature can reach more than 75 °C [42]). Therefore, to

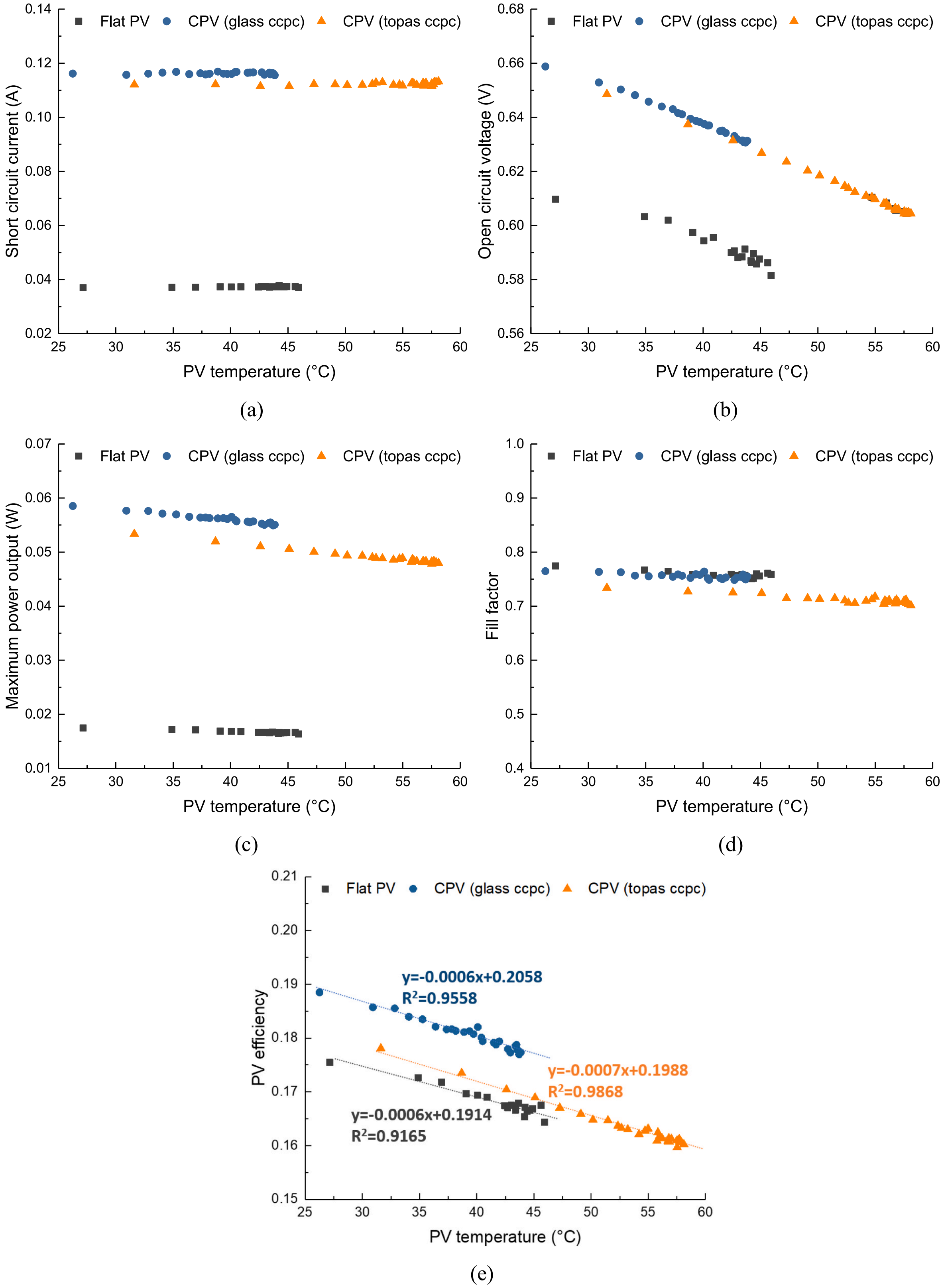

(a) (b) (c) (d) (e)

Fig. 8. Relations between PV temperature and (a) short circuit current, (b) open circuit voltage, (c) maximum power output, (d) fill factor, and (e) PV efficiency.

accurately calculate the SHGC of the glazing system containing complex optics and PV cells, all the above issues need to be solved.

$$SHGC = \tau + N \times \alpha + N' \times \eta_{op} \times (1 - \eta_{pv}) \tag{2}$$

Where, η_{op} is the optical efficiency of the CCPC-PV window. η_{pv} is the PV conversion efficiency. N' is the inward-flowing fraction for heat released by PV.

This study is going to develop a comprehensive model to characterise the optical, thermal, and electrical performance of complex PV window

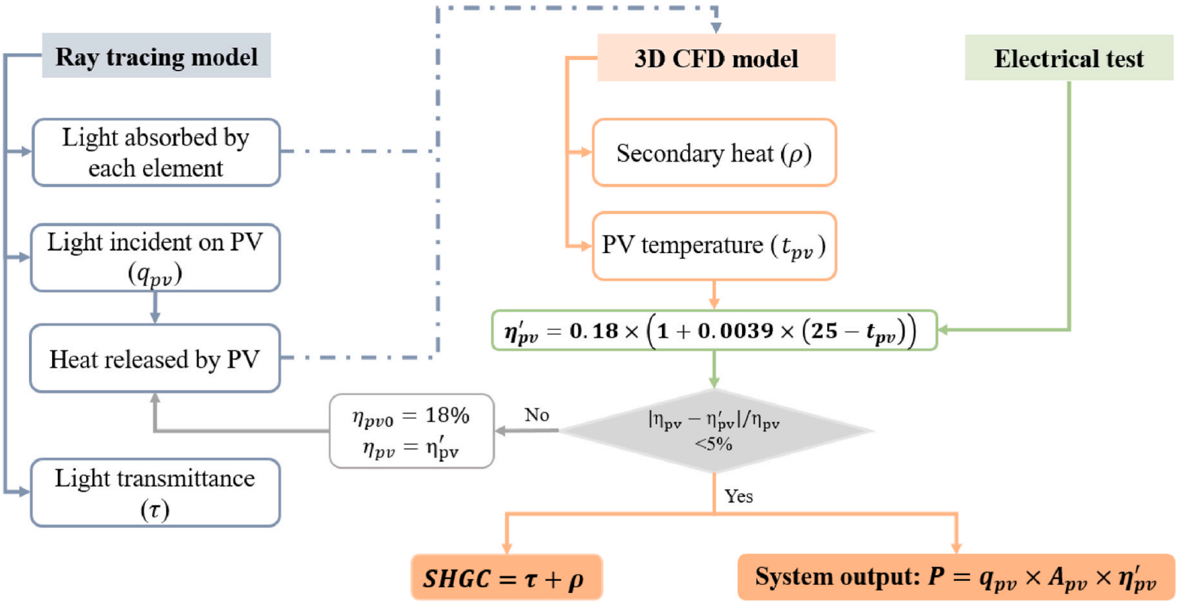

Fig. 9. Procedure for inputting the ray-tracing simulation results and electrical test results into the CFD simulation.

Table 4
Material properties of the CCPC-PV window [11,45,46].

Material	Property	Unit	Value
Air	Specific heat capacity	J/kg·K	1005
	Conductivity	W/m·K	0.025
	Expansion coefficient	1/K	0.00353
Topas (Polyolefin/Zeonex: COC Polymer)	Conductivity	W/m·K	0.11
	Emissivity	–	0.84
	Thickness	mm	2(f)+16.16(p)
Glass pane	Conductivity	W/m·K	1.4
	Emissivity	–	0.84
	Thickness	mm	4
PV cell	Conductivity	W/m·K	149
	Thickness	m	0.0004
Sylgard 184	Conductivity	W/m·K	0.16
	Thickness	mm	1.5

systems at different environmental conditions e.g., due to sun's altitude and azimuth. A Crossed Compound Parabolic Concentrating Photovoltaic (CCPC-PV) window has been selected as an example for this study. To do this, a framework for combining a ray-tracing model and Computational Fluid Dynamics (CFD) model was proposed and the model development as well as the validation of the ray-tracing model and CFD model were undertaken. Meanwhile the electrical characterisation of the Concentrating PV (CPV) system has been obtained through indoor tests. The validated models were then used to simulate temperature profiles (e.g., PV temperature and window temperature) and secondary inward heat of the CCPC-PV window. To accurately predict the system output, the PV conversion efficiency was updated based on the simulated PV temperature. Finally, the SHGC and power output (as determined in this study) along with the U-value and light transmittance (obtained in our recent work by Li et al. (2023) [43]) for the CCPC-PV window and its various designs, were presented and compared to a similarly structured double-glazed system.

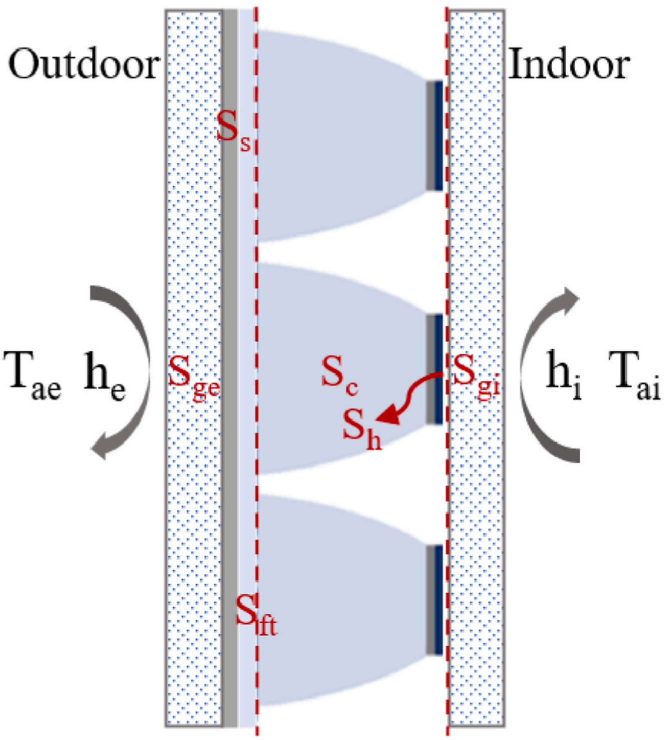

Fig. 10. Boundary conditions for CFD modelling (a 3 × 3 prototype for an example).

2. Research methodology

To accurately predict the optical (light transmittance and light absorptance), thermal (PV temperature, window temperature and secondary heat) and electrical (power output) performance of the glazing system containing complex structures and PV cells, such as the CCPC-PV window, this section outlines a procedure based on the combined CFD and ray-tracing method, as illustrated in Fig. 1. A ray-tracing model was developed and validated in **Section 2.2** to simulate the light transmittance of the CCPC-PV window as well as the solar energy absorbed by

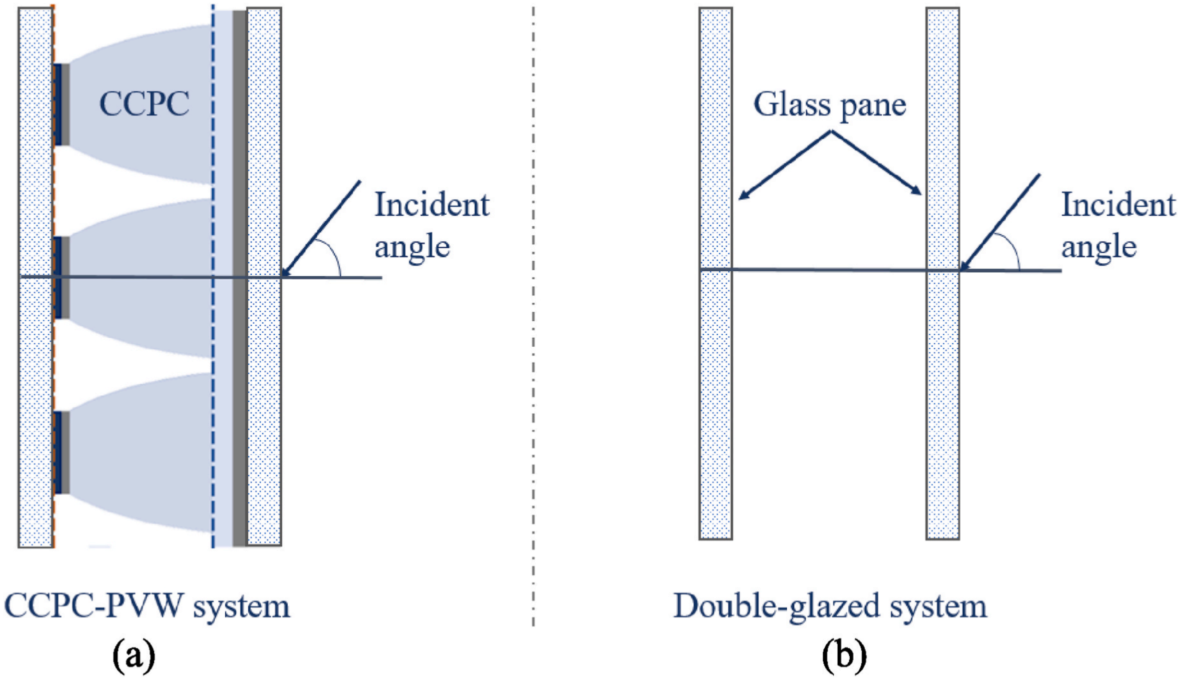

Fig. 11. Incident angle of the (a) CCPC-PV window and (b) a similar structured double-glazed system.

each solid-element and PV cells. To estimate the heat released by PV power generation for inputting into a CFD model for window thermal characterisation later, an electrical test was conducted in **Section 2.3** to obtain the electrical characteristics of the PV cell within the CCPC-PV window, such as the PV conversion efficiency at standard test condition (1000 W/m^2, AM 1.5, 25 °C) and temperature coefficient. Finally, a CFD model was established and validated in **Section 2.4**. The results from the ray-tracing simulation and electrical tests, such as the solar energy absorbed by each element into the CCPC-PV window and the heat released from PV power generation were input into the validated CFD model as boundary conditions to obtain the temperature profile (e.g., PV temperature and window temperature) and secondary heat of the CCPC-PV window. The power output of the CCPC-PV window was calculated from the solar energy incident on the PV surfaces and the final updated PV efficiency based on the simulated cell temperature. Following National Fenestration Rating Council (NFRC) standard [44], the other boundary conditions for those simulations were determined to obtain the SHGC of fenestration products at normal incidence condition as listed in Table 1.

2.1. *CCPC-PV window*

The window sample with dimensions of 600 mm (height) × 600 mm (width) × 28.06 mm (glazing thickness) × 80 mm (aluminium frame thickness), as shown in Fig. 2 (a), was provided by the University of Exeter, UK [45,46]. The Crossed Compound Parabolic Concentrator Photovoltaic (CCPC-PV) window consists of 81 3 × 3 CCPC-PV modules (Fig. 2 (b)) arranged in a matrix of 9 × 9 sandwiched between two 4 mm-thick glass panes. The cross-sectional view of the CCPC-PV window, along with its detailed configuration, is depicted in Fig. 2 (c). From the outer layer to the inter layer, it consists of 4 mm-thick float glass pane top, 1.5 mm-thick silicone encapsulant (Sylgard 184), 18.16 mm CCPC optics (2 mm flat joining layer + 16.16 mm parabolic shaped optics), 0.2 mm-thick Sylgard 184, 0.2 mm-thick crystalline silicon solar cells (1 cm^2 area for each cell) and 4 mm-thick float glass pane bottom. Fig. 2 (d) illustrates the geometry of a single CCPC optic with a geometric concentration ratio of 3.6.

For the original CCPC-PV window design, the horizontal and vertical pitches between two adjacent CCPC entry apertures are 1.77 mm. In addition to the original design, different horizontal pitches (D_x) and vertical pitches (D_y) were explored to study their effects on the overall window performance.

2.2. *Ray-tracing model*

This section provides detailed information of the ray-tracing model established using commercial software, TracePro. In the simulation, incident rays were considered as beam radiation, in other words, all the rays entering the CCPC-PV window contained the same amount of energy and were spaced evenly. Based on the ray independence test as demonstrated in Table 2, 119401 rays were applied on the entry surface of the CCPC-PV window. The solar irradiance was set as 783 W/m^2 (Table 1) for the solar grid source and the spectrum was simplified to a single wavelength of 0.5461 μm. The optical properties of the materials used in the CCPC-PV window at single-wavelength spectrum can be found in Table 3.

Fig. 4 illustrates the symmetry property of one CCPC optic, which is also consistent across the entire CCPC-PV window. There are four planes of symmetry including the East-West (E-W) plane, North-South (N–S) plane and two diagonal planes (NE-SW and NW-SE) and the angle between the diagonal plane and N–S plane or E-W plane is 45°. Rays from different planes can be transferred into a range from 0° (N–S) to 45° (NE-SW) as all of the incident rays are symmetric about these four planes, which have the same light behaviour into the CCPC optic and CCPC-PV window. In this study, simulations were conducted at different incident angles from 0° to 90° with 10° interval and different plane angles from 0° to 45° with 15° interval.

The developed ray-tracing model was also validated with small CPV prototypes using a spectrometer and solar simulator under indoor conditions, as illustrated in **Appendix 1**. After the model validation, the established CCPC-PV window model with dimensions of 600 mm (length) × 600 mm (height) × 28.06 mm (thickness) was used to simulate the detailed solar-optical properties including the solar energy absorbed by each solid element and solar cells. Fig. 5 shows the light flow through a 3 × 3 CCPC-PV window prototype. The solar energy absorbed by the CCPC-PV window includes A_{ge} for external glass pane,

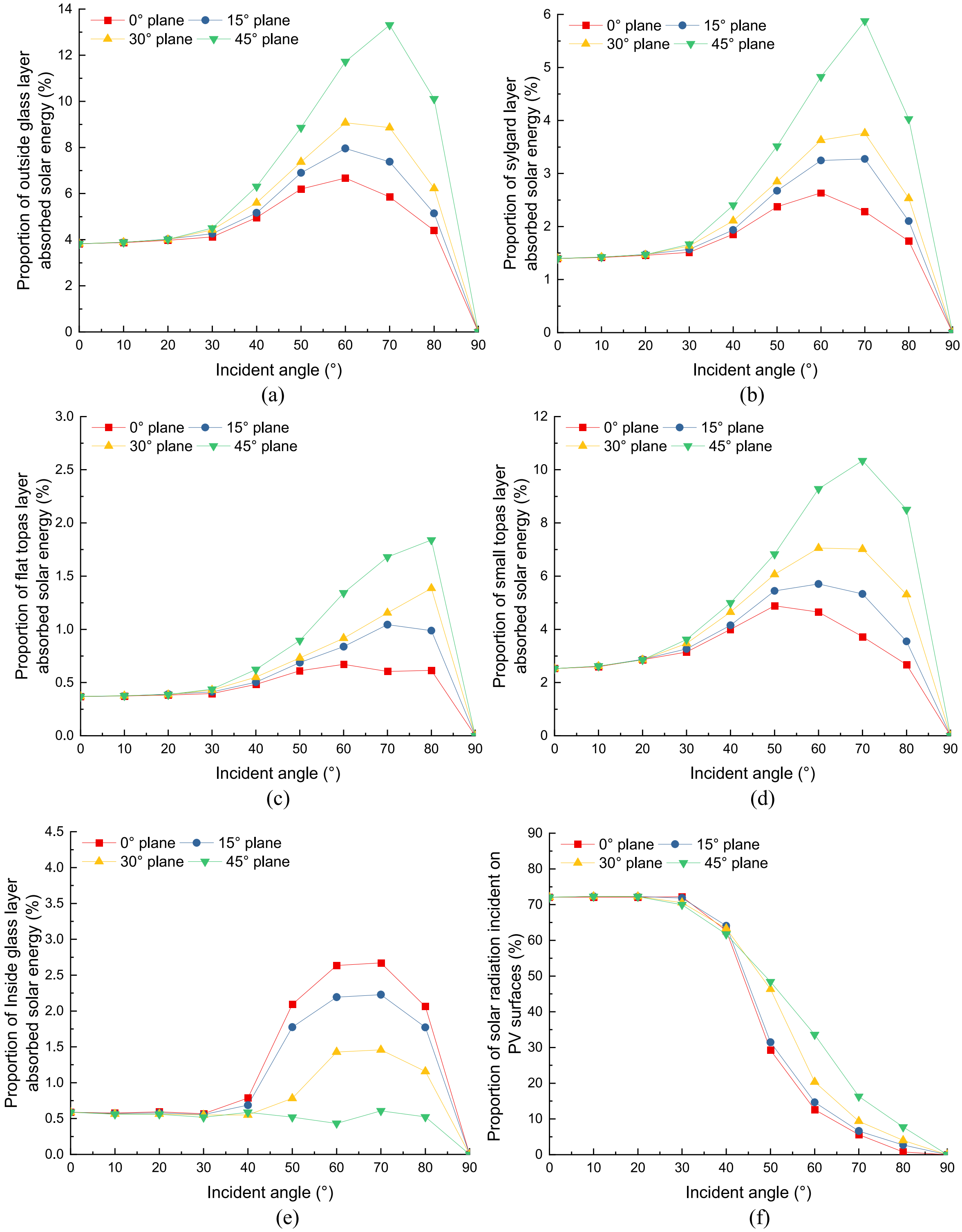

Fig. 12. Proportion of (a) outside glass layer, (b) sylgard layer, (c) flat topas layer, (d) CCPC optics, (e) indoor glass layer, and (f) PV cells absorbed solar energy on the total solar energy incident on the window outside.

A_s for flat sylgard layer, A_{ft} for flat topas layer, A_c for CCPC optics, A_{gi} for internal glass pane as well as those absorbed by PV cells ($Q_{pv} = Q_e + Q_h$) (Q_e represents the generated power while Q_h represents the released heat). The ray-tracing simulation results for the CCPC-PV window and its various designs can be found in Section 3.1, which will be ultimately input into the CFD model in Section 2.4 for thermal characterisation.

2.3. *Electrical characterisation of CPV*

The validated ray-tracing model as described in the last section can be used to simulate the amount of optical flux absorbed by each solid element and the PV cells within the CCPC-PV window. However, to estimate the heat dissipation from the PV power generation for inputting into the CFD model (Section 2.4) for thermal characterisation, the electrical characteristics, such as the PV conversion efficiency at

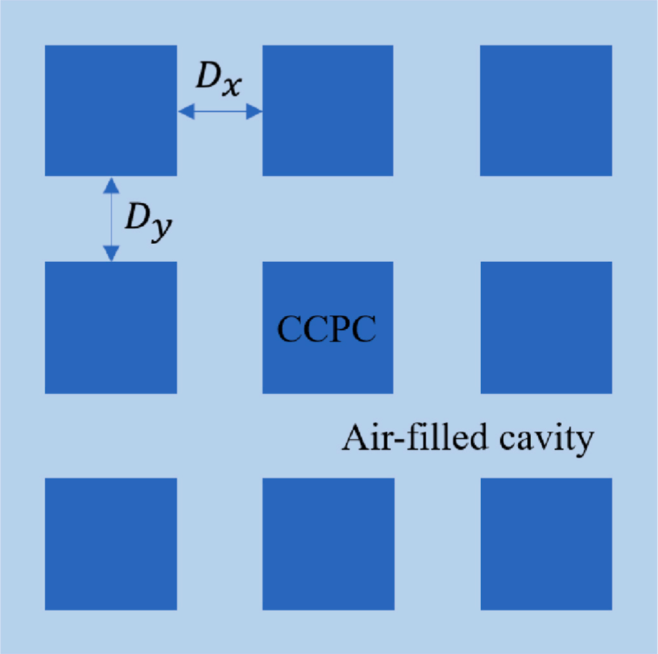

Fig. 13. Horizontal pitch (D_x, mm) and vertical pitch (D_y, mm) between adjacent CCPC optics into a 3 × 3 CCPC-PV window prototype.

standard test condition (1000 W/m^2, AM 1.5, 25 °C) as well as the temperature coefficient need to be obtained before the CFD simulation. In this section, the glass CPV and topas CPV (without B270 covers) as shown in Fig. A1-3 (**Appendix 1**) were used as samples. The indoor test setup as shown in Fig. A1-2 (**Appendix 1**) was used to conduct the electrical test. Temperature control was implemented to ensure the PV temperature gradually increased to exceed 40 °C. The whole test lasted around 10 min and I–V curves of the PV cells were retrieved every 20 s.

The simulated I–V and P–V curves under different PV temperatures and 1000 W/m^2 solar radiation are illustrated in Figs. 6 and 7 for the glass CPV, topas CPV and a bare PV cell. The short circuit current remains relatively constant across different cell temperatures while the maximum power point and open circuit voltage point shift downwards as the operating temperature of the PV cell increases from the room temperature to over 40 °C. The open circuit voltage decreases from 0.659 V to 0.631 V for the glass CPV, from 0.649 V to 0.604 V for the Topas CPV, and from 0.610 V to 0.582 V for the bare PV cell during the test. The corresponding maximum power output decreases from 0.059 W to 0.055 W for the glass CPV, from 0.053 W to 0.048 W for the Topas CPV, and from 0.017 W to 0.016 W for the bare PV cell, respectively.

Based on above I–V and P–V curves at different cell temperatures, the relations between PV temperature and short circuit current, open circuit voltage, fill factor and PV efficiency are depicted as shown in Fig. 8. It is obvious that the PV temperature only has a slight effect on the short circuit current for the PV cell with different optics/no optic attached as mentioned before. The open circuit voltage, maximum power output, fill factor and PV efficiency all decrease linearly with the increase of the PV temperature. As anticipated, the glass CPV produces the highest maximum power output. A slight decrease in the maximum power output (around 0.005 W) for the topas CPV is attributed to the higher light absorption of the topas material and the lower quality optical finish of the PV concentrator. Given that the glass CPV has higher optical efficiency than the topas CPV and considering that PV efficiency increases with higher incident irradiance on the PV surface (optical efficiency), the PV cell attached to a glass concentrator exhibits a higher conversion efficiency (19.1 %) tcompared to the PV cell attached to a topas concentrator (18.1 %) at a cell temperature of 25 °C. The corresponding data for the bare PV cell was calculated as 17.6 %. The temperature coefficients (δ) were predicted as 0.0031/°C, 0.0039/°C and 0.0034/°C for the PV cell attached to a glass concentrator, topas concentrator and no concentrator, respectively. The PV conversion efficiency (η_{pv}) at specific PV temperature (t_{pv}) can be calculated based on the standard PV conversion efficiency at 25 °C (η_{st}) and temperature coefficient (δ) according to Eq. (3). This relation was used to estimate the heat released by PV power generation for inputting into the CFD model to conduct the thermal characterisation in the next section.

$$\eta_{pv} = \eta_{st}\left(1 + \delta \times \left(25 - t_{pv}\right)\right) \tag{3}$$

2.4. *Computational fluid dynamics model*

Before delving into the development of the CFD model, the process of incorporating the simulation results from the ray-tracing model in **Section 2.2** and the measured PV characteristics from the electrical test in **Section 2.3** into the CFD model for thermal characterisation is illustrated in Fig. 9. Based on the ray-tracing simulation, the light transmittance (τ), solar energy absorbed by the CCPC-PV window as well as the solar energy incident on the PV cells can be obtained. For the CCPC-PV window installed in a building, a portion of the solar energy absorbed by each element of the CCPC-PV window, along with the heat released by PV power generation, will enter the indoor space through convection and radiation. These factors collectivelty contribute to the secondary inward heat. To estimate this secondary heat, those absorbed and released heat were converted as volume heat sources and then input into a CFD model as boundary conditions. The PV conversion efficiency (η_{pv}) was initially assumed to be the value at standard test condition (18 %) at the beginning of the simulation to estimate the heat released by PV cells. Iw was then iterated based on the relationship between the simulated PV temperature (t_{pv}) and the PV conversion efficiency ($\eta_{pv}^{'}$), as determmined through the electrical test described in **Section 2.3**. The final updated PV efficiency was used to estimate the system's output.

In this section, a three-dimensional finite volume model for thermal characterisation of the CCPC-PV window was developed in the commercial CFD package FLUENT 19.1. To simplify the CFD simulation process, the following assumptions were made: (1) The enclosure was filled with air with Pr = 0.71, all thermophysical properties (e.g., c_p, λ) of the fluid were assumed to be constant, except for the fluid density and viscosity, which varied with temperature. (2) The flow inside the air cavity formed by CCPC optics keeps laminar as the Grashof (Gr) Numbers never reach the related critical value [47,48]. (3) The Surface to Surface (S2S) radiation model was used to solve the radiative transfer equation between the internal surfaces. (4) The window geometry with a CCPC-PV matrix of 1 × 27 rather than 27 × 27 was used to establish the mesh. The left and right surfaces were set as symmetry while the top and bottom surfaces were set as adiabatic.

The material properties for the developed window model are listed in Table 4, and Fig. 10 shows its boundary conditions. The window indoor and outdoor air temperatures and surface heat transfer coefficients were set based on NFRC standard (Table 1). In addition, the absorbed solar energy (A_{ge}, A_s, A_{ft}, A_c and A_{gi} in Fig. 4) and heat dissipated by PV power generation (Q_h in Fig. 4) were assigned as volume heat sources (S_{ge}, S_s, S_{ft}, S_c, S_{gi}, and S_h) to each solid element in the CCPC-PV window model. Detailed information on model validation and power output prediction can be found in **Appendix 2**.

As mentioned before, the SHGC value of the CCPC-PV window can be calculated using Eq. (2). In this equation, the light transmittance (τ) can be obtained through ray-tracing simulation, as described in **Section 2.2**. The rest of the terms on the right side of this equation, which was defined as $\rho = N \times \alpha + N^{'} \times \eta_{op} \times (1 - \eta_{pv})$, can be calculated using Eq. (4).

$$\rho = \frac{Q_{withrad} - Q_{withoutrad}}{Q_{in}} \tag{4}$$

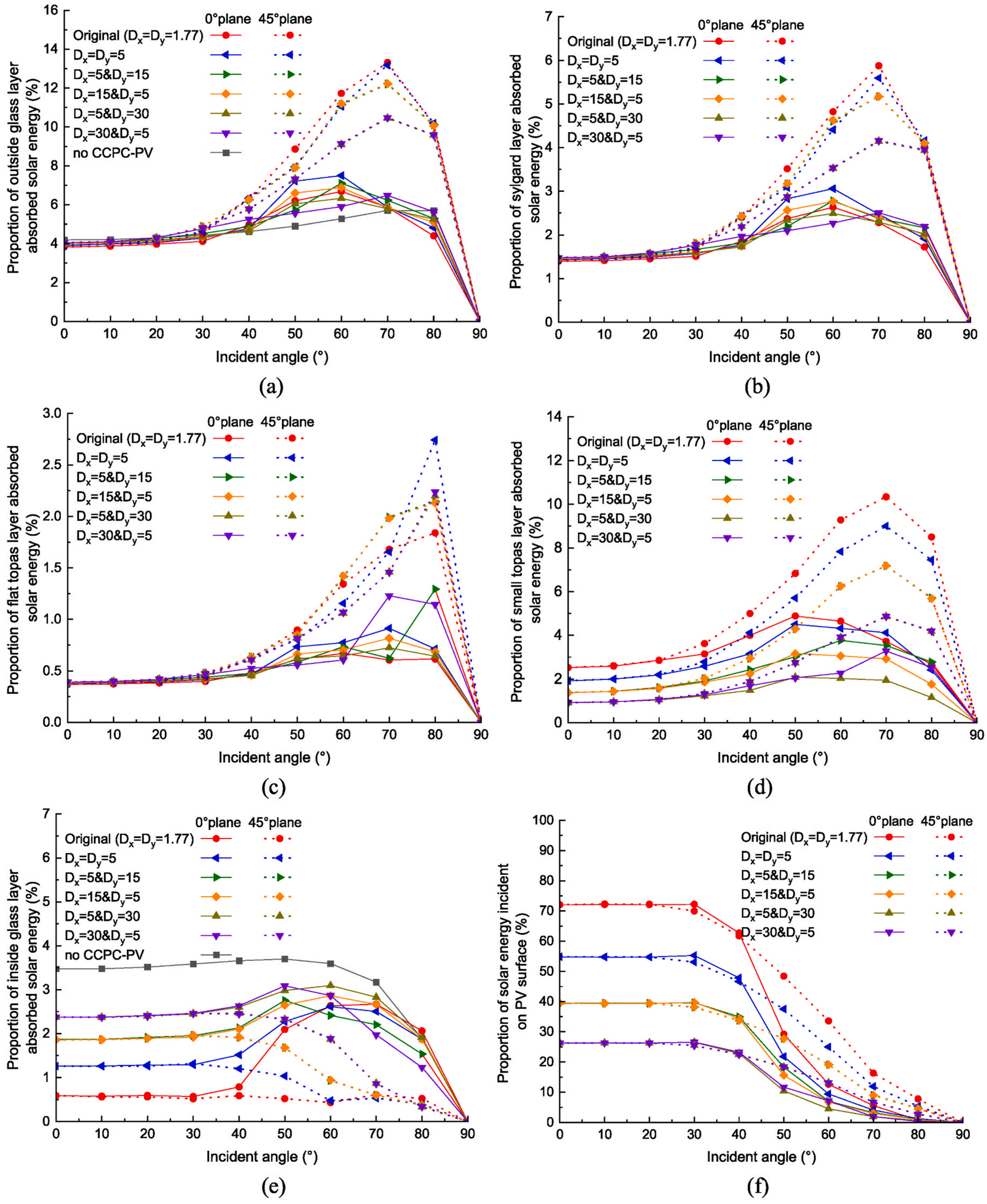

Fig. 14. Proportion of (a) outside glass layer, (b) sylgard layer, (c) flat topas layer, (d) CCPC optics, (e) indoor glass layer, and (f) PV cells absorbed solar energy on the total solar energy incident on the window outside.

where, $Q_{withrad}$ is the total heat flux inward to the indoor space through convective and radiative heat transfer for the case of solar radiation from outside, including the heat absorbed by each element, heat released by PV and heat flux driven by indoor and outdoor air temperature difference (thermal transmittance or U-value), measured in watts (W). $Q_{withoutrad}$ is the value for the case of no radiation, the heat flow through the window only due to thermal transmittance (U-value), measured in watts (W). And Q_{in} is the total solar radiation incident on the window outside surface, measured in watts (W). $Q_{withrad}$ and $Q_{withoutrad}$ can be obtained from the CFD simulation for scenarios involving solar radiation from outside (where volume heat sources are incorporated into each solid element of the system) and for the scenarios without radiation, respectively.

3. Results and discussion

In this section, the optical, thermal and electrical performance of the CCPC-PV window and its various designs are presented at different incident angles from various planes. The solar-optical properties of the CCPC-PV window, essential for for inputting into the CFD model for

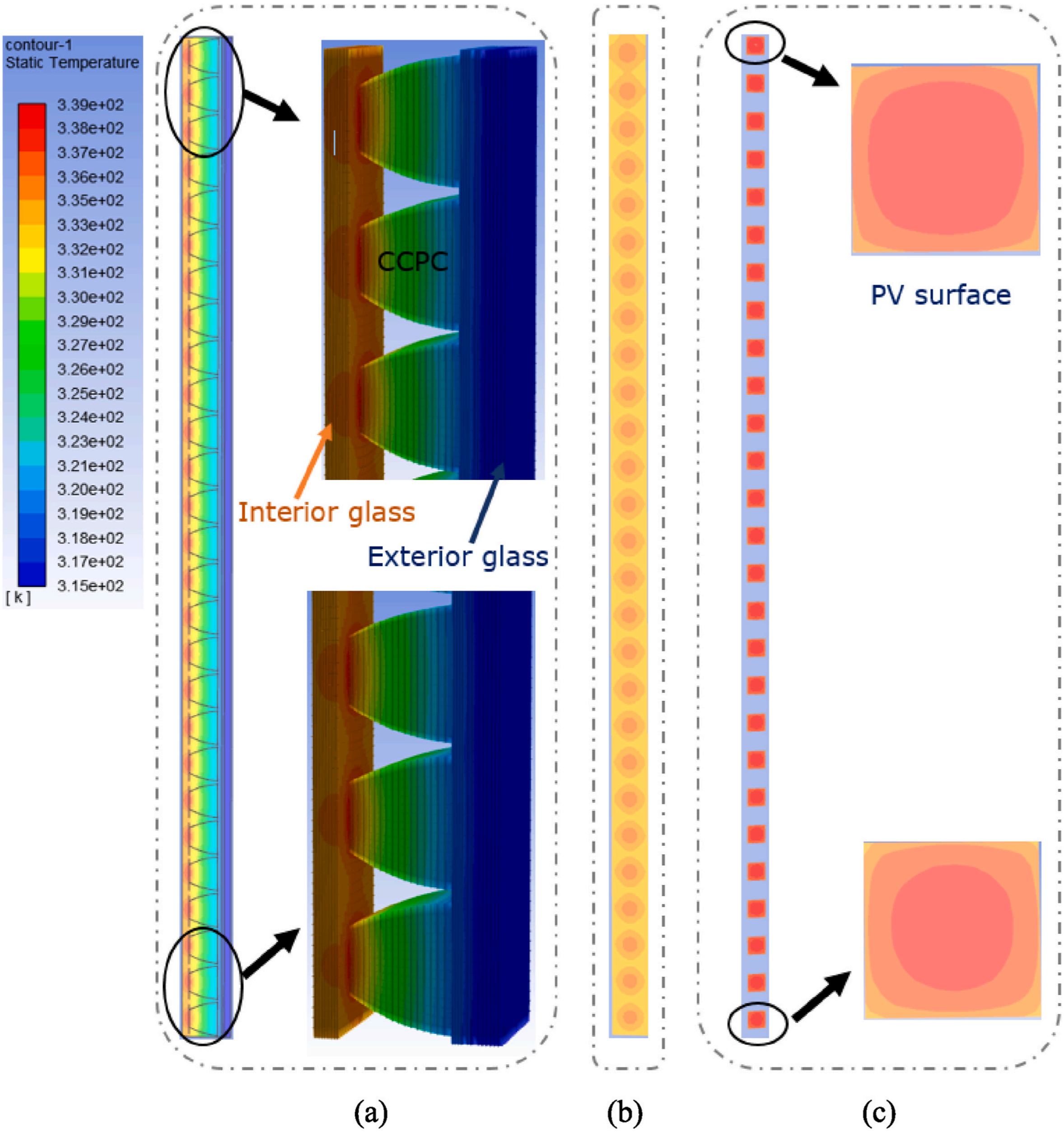

Fig. 15. (a) Temperature profile of the CCPC-PV window, (b) window inside surface temperature, and (c) PV surface temperature at 0° incident angle.

thermal characterisation, such as the solar energy absorbed by each element and PV cells into the CCPC-PV window are presented initially.. Following this, the detailed thermal and energy performance of the CCPC-PV window, including aspects like PV temperature, window temperature, secondary heat, SHGC and system output are discussed and compared with a similarly structured double-glazed system.

3.1. *Ray-tracing results*

In this section, the solar-optical properties are presented for the original CCPC-PV window first, followed by the results with various designs. The data primarily includes the proportion of solar energy absorbed by each solid element and PV cells relative to the total solar energy incident on the window's outside surface. These absorbed energy terms were then converted into volume heat sources and input into the CFD model as boundary conditions for thermal characterisation (results can be found in Section 3.2).

3.1.1. *Solar energy absorbed by original CCPC-PV window*

Fig. 11 shows the incident angle of the CCPC-PV window (a 3 × 3 prototype) and a similar structured double-glazed system. Fig. 12 (a-e) illustrates the proportion of solar energy absorbed by each element relative to the total solar energy incident on the window outside surface at different incident angles from various planes. All proportions increase first then decrease as the incident angle increases from 0° to 90° with most peak values occurring between 60° and 80°. A higher proportion of absorbed solar energy occurs at higher plane angle, except for the inside glass layer. Fig. 12 (f) shows that the proportion of solar energy incident on the PV surface gradually decreases as the incident angle increases from 0° to 90°. A higher plane angle yields a larger proportion value for incident angle between 40° and 80°.

3.1.2. *Solar energy absorbed by CCPC-PV window with various designs*

This section presents data for the window with a CCPC-PV structure featuring various horizontal pitches (D_x) and vertical pitches (D_y) as illustrated in Fig. 13. Fig. 14 displays the proportions of solar energy

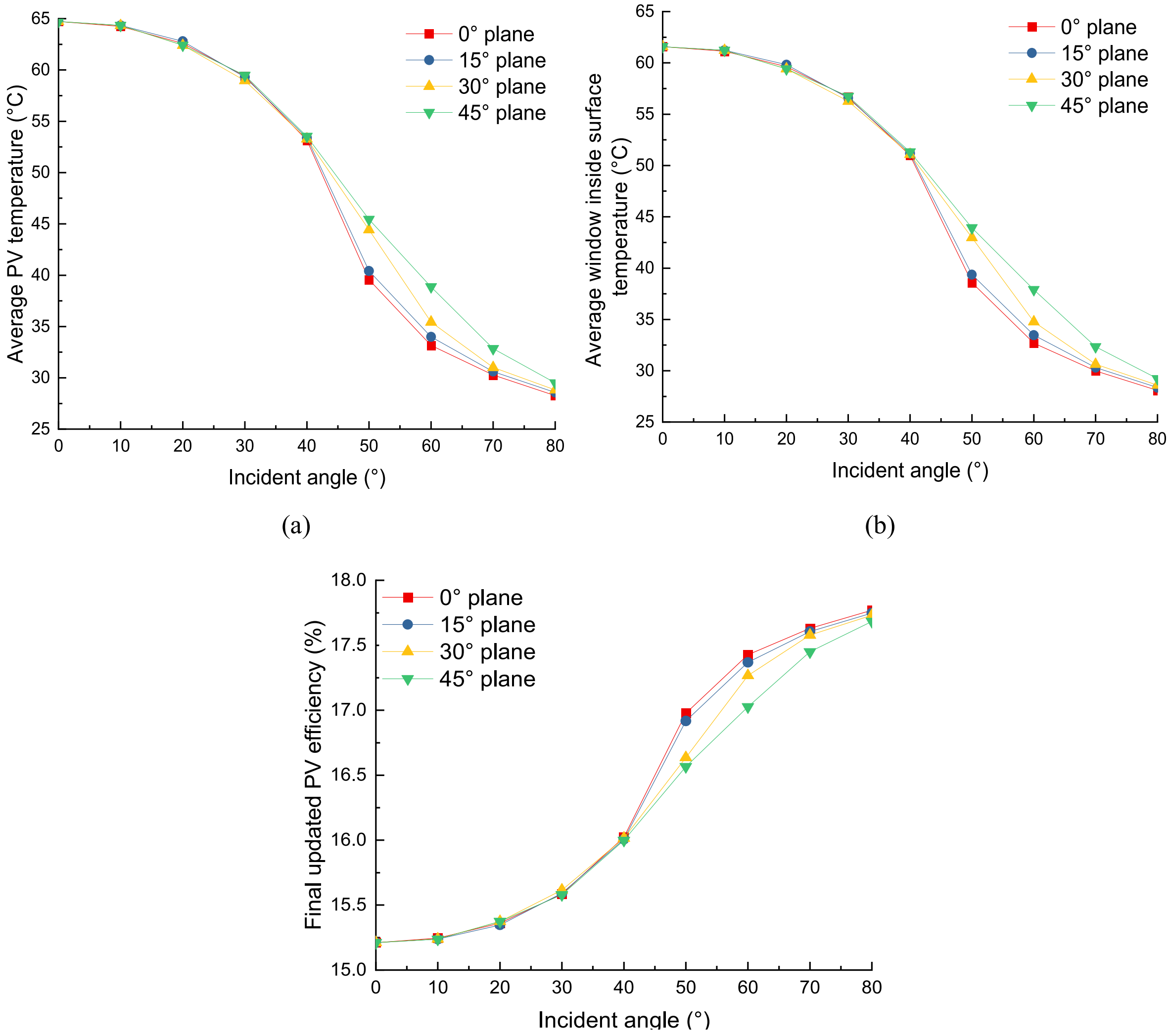

(a)

(b)

(c)

Fig. 16. (a) Average PV surface temperature, (b) average window inside surface temperature, and (c) finial updated PV efficiency.

absorbed by the front three flat layers, CCPC optics, inside glass layer, and PV cells for solar rays originating from planes ranging from 0° to 45°. As the pitch between adjacent CCPC optics increases, the number of PV cells within the window decreases, leading to a reduction in the proportion of incident rays absorbed by PV cells.

3.1.3. Summary

Based on the ray-tracing simulation results for the original CCPC-PV window, it can be seen that the PV cells within the CCPC-PV window can absorb a large proportion (more than 70 % at 0° incident angle) of solar energy incident on the window. Other solid elements, including the outdoor glass layer, sylgard layer, flat topas layer, CCPC optics, and indoor glass layer, all absorbed less than 15 % of total solar energy incident on the window at various incident angles. As the horizontal (D_x)/vertical pitch (D_y) between adjacent CCPC optics increased from 5 mm to 30 mm, the proportion of solar energy incident on the PV surfaces decreased from 55 % to 26 % (at 0° incident angle) because of the reduced number of CCPC-PV units within the window system. The corresponding proportions of solar energy absorbed by the other solid elements remained low for these newly designed windows as well. A small portion (less than 18 %) of solar energy absorbed by the PV cells within the window is converted into electrical power, while the majority is released in the form of heat, which then contributes to the the window's heat transfer process. Therefore, to thermally characterise the CCPC-PV window in scenarios involving solar radiation from outside, all absorbed solar heat terms must be input into the CFD model to conduct the thermal modelling. The results are presented in the following section.

3.2. CFD results for thermal characterisation of the CCPC-PV window

For the thermal characterization of the CCPC-PV window, typical heat transfer boundary conditions (air temperature, t_{ai}, t_{ae} and surface heat transfer coefficient, h_i and h_e) specified in the NFRC standard [44] for SHGC simulation, along with the solar energy absorbed by each element within the window, were applied to the CFD model. This section provides a detailed thermal performance, including the PV temperature, window inside surface temperature and the final updated PV efficiency for the original CCPC-PV window first. Subsequently, the performance data for the CCPC-PV window with various designs is presented.

3.2.1. Temperature profile of original CCPC-PV window

Fig. 15 shows the temperature profile of the original CCPC-PV window at 0° incident angle. Because the conduction dominates the heat transfer and the effect of the convection is small, there is no significant (air temperature, PV temperature and window inside surface temperature) temperature gradient over height. Fig. 16 shows the average PV surface temperature, average window inside surface temperature and

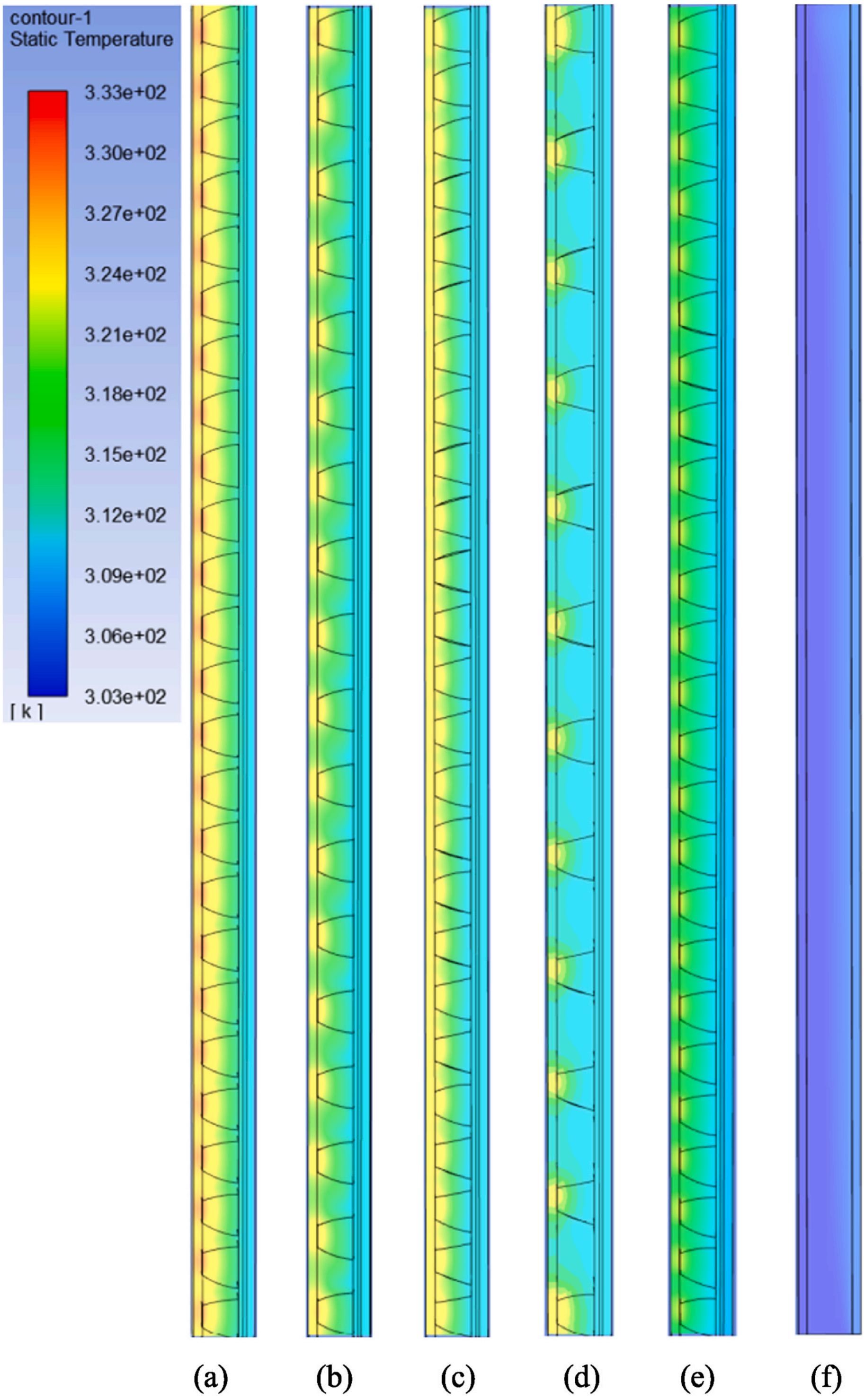

Fig. 17. Temperature profile of the window with a CCPC-PV structure of (a) $D_x = D_y = 5$, (b) $D_x = 5$ & $D_y = 15$, (c) $D_x = 15$ & $D_y = 5$, (d) $D_x = 5$ & $D_y = 30$, (e) $D_x = 30$ & $D_y = 5$, and (f) no CCPC-PV at 0° incident angle (D_x and D_y are horizontal and vertical pitches, mm).

the final updated PV efficiency at different incident angles from various planes. The average PV surface temperature gradually decreases with the increase of the incident angle and is higher at a larger plane angle for the incident angle between 40° and 80° (Fig. 16 (a)). This occurs because a larger plane angle results in more solar energy incident on the PV surface for incident angles between 40° and 80° (as shown in Fig. 12 (f)). The average temperature of the window’s inside surface shows the same variation as the PV temperature across all incident angles and planes (Fig. 16 (b)). Fig. 16 (c) shows that the final updated PV efficiency gradually increases as the incident angle rises from 0° to 90°. Additionally, the efficiency is higher for lower plane angle when the incident angle ranges between 40° and 80°. This tendency is contrary to that of the PV temperature, as the PV efficiency is higher when the PV temperature is lower.

3.2.2. *Temperature profile of CCPC-PV window with various designs*

Fig. 17 shows the temperature profile of the CCPC-PV window with various designs at 0° incident angle. The average PV temperature,

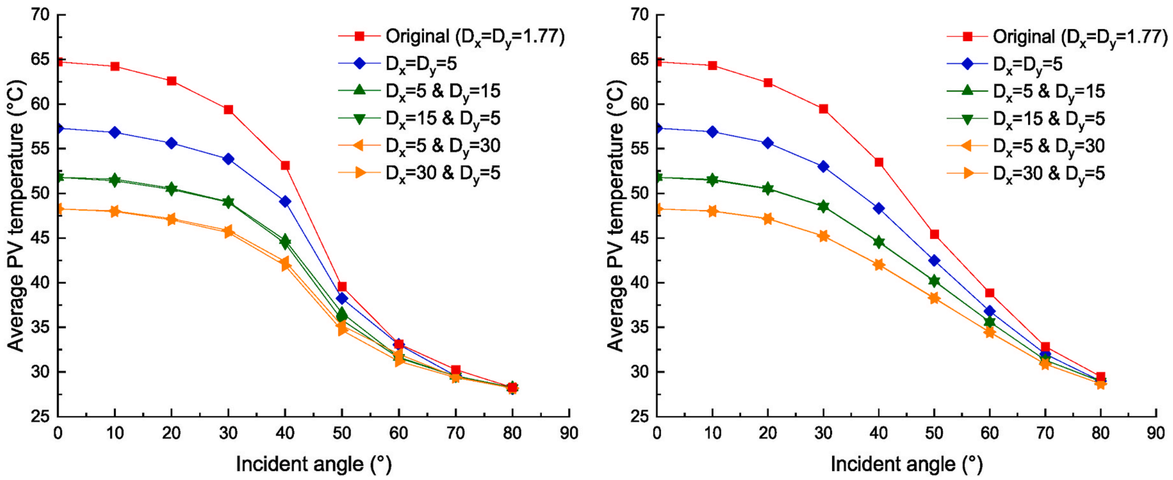

(a) 0° plane

(b) 45° plane

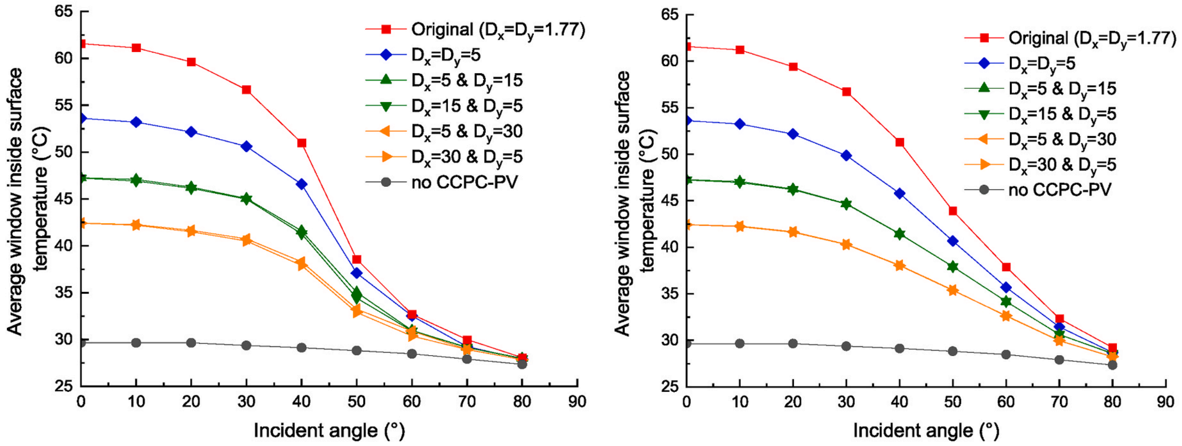

(c) 0° plane

(d) 45° plane

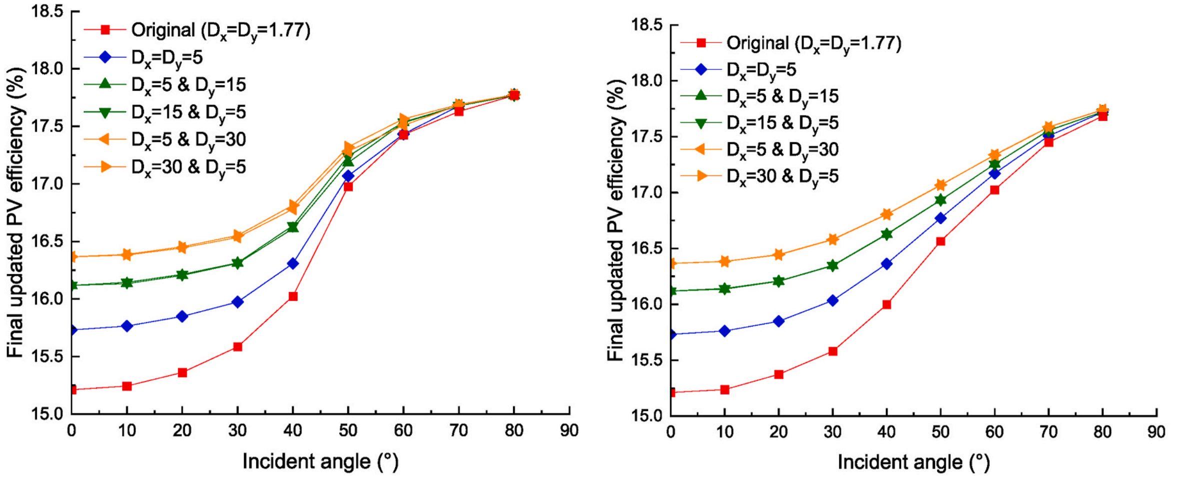

(e) 0° plane

(f) 45° plane

Fig. 18. (a) Average PV temperature, (c) average window inside surface temperature and (e) finial updated PV efficiency for solar rays from 0° plane and the corresponding data (b), (d), and (f) for solar rays from 45° plane (D_x and D_y are horizontal and vertical pitches, mm).

average window inside surface temperature and final updated PV efficiency of the CCPC-PV window at different incident angles from various planes can be found in Fig. 18. As the pitch between adjacent CCPC optics increases, both the average PV temperature and window inside surface temperature decrease due to less heat released from PV power generation (Fig. 18 (a)–(d)). The final updated PV efficiency for a sparser configuration is higher because of a lower PV temperature (Fig. 18 (e) and (f)).

3.3. SHGC of the CCPC-PV window

As mentioned before, the SHGC value consists of the directly transmittance part and secondary heat part. The light transmittance of the CCPC-PV window and its various designs (Fig. A3-1to Fig. A3-3 in

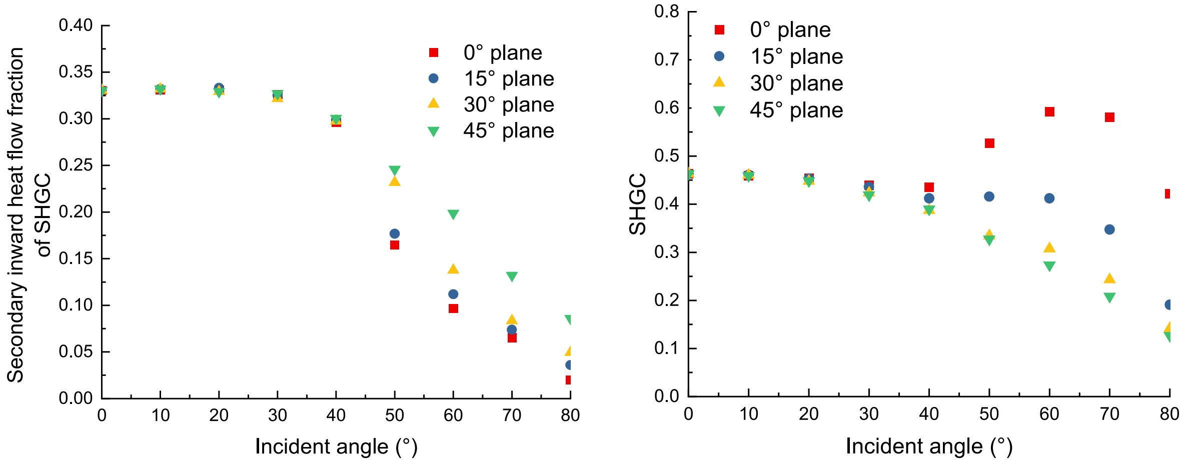

(a) (b)

Fig. 19. (a) Secondary inward heat and (b) SHGC of the CCPC-PV window.

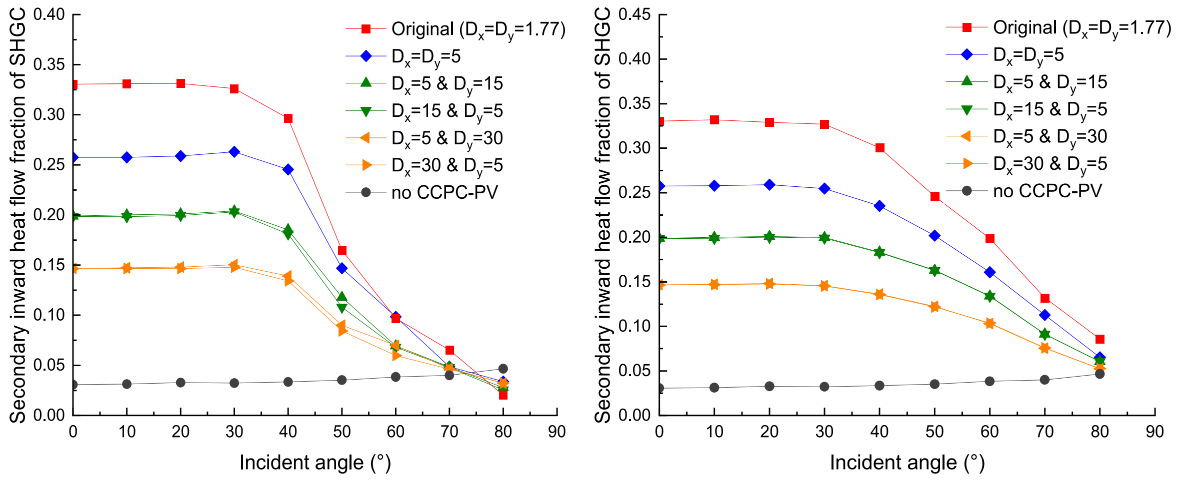

(a) 0° plane

(b) 45° plane

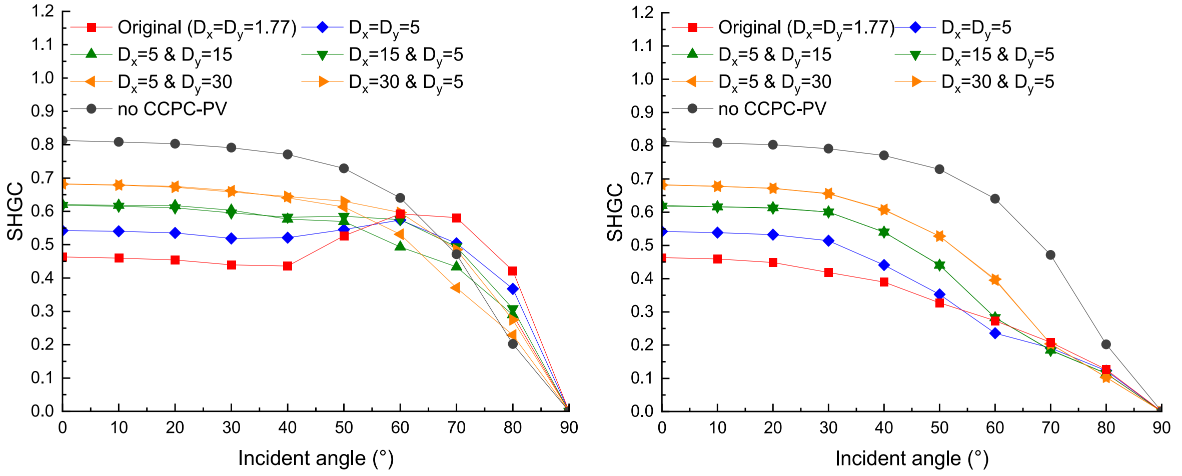

(c) 0° plane

(d) 45° plane

Fig. 20. (a) Secondary inward heat and (c) SHGC of CCPC-PV window for solar rays from 0° plane and the corresponding data (b) and (d) for solar rays from 45° plane (D_x and D_y are horizontal and vertical pitches, mm).

Appendix 3) was investigated in our recent work by Li et al. (2023) [43]. This section first presents the secondary heat and SHGC of the original CCPC-PV window. Subsequently, it provides the data for the CCPC-PV window with various designs at different incident angles from various planes.

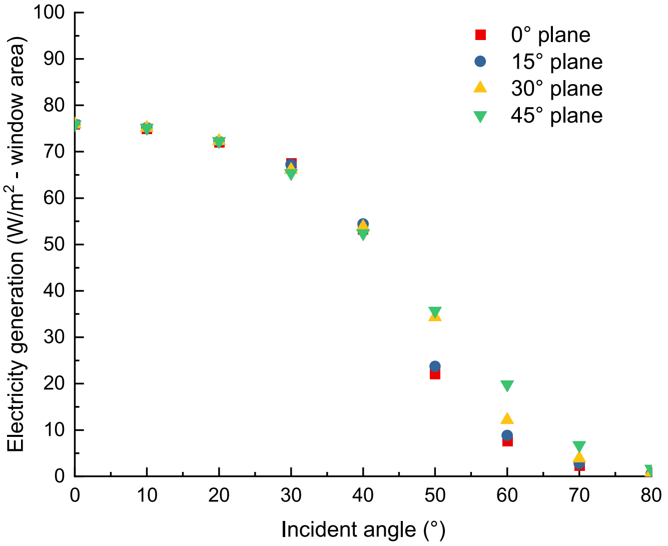

Fig. 21. Power output of the CCPC-PV window.

3.3.1. *SHGC of original CCPC-PV window*

Fig. 19 (a) shows the secondary inward heat fraction of the SHGC under different incident angles from various planes. The proportion of secondary heat decreases gradually from 0.33 to around 0.05 as the incident angle increases from 0° to 80°. And it is lager for a higher plane angle when the incident angle is between 40° and 80°. Fig. 19 (b) shows the SHGC of the CCPC-PV window at different incident angles from various planes. The highest SHGC value (0.59) occurs at 60° incident angle from 0° plane because of the highest light transmittance (0.50).

3.3.2. *SHGC of CCPC-PV window with various designs*

Fig. 20 shows the secondary heat and SHGC of the CCPC-PV window with various designs. Similar to those with original configuration, the fraction of secondary heat is higher for solar rays originating from a 45° plane angle, especially when the incident angle ranges from 40° to 80°. As the pitch between adjacent CCPC optics increases, the fraction of secondary inward heat decreases because of the reduced amount of PV released heat. In addition, the secondary heat of the double-glazed window is much lower than that of the CCPC-PV windows, only accounting for less than 5 % of the total solar radiation incident on the exterior window surface. The SHGC value is more affected by the light transmittance (as shown in Fig. A3-1to Fig. A3-3 in **Appendix 3**) than the secondary heat. For example, the SHGC value of the double-glazed window is higher than that of various CCPC-PV windows at most incident angles from 0° to 45° plane, due to its high light transmittance. The window with a sparser CCPC-PV structure (e.g., D_x = 5 mm & D_y = 30 mm and D_x = 30 mm & D_y = 5 mm) exhibits a higher SHGC due to greater light transmittance when the incident angle is less than 50°. Conversely, it has a lower SHGC due to reduced light transmittance when the incident angle exceeds 50°.

3.4. *Power output of the CCPC-PV window*

In this section, the power output of the original CCPC-PV window is presented first, based on the ray-tracing results of the solar energy incident on the PV surfaces and the CFD results of the PV temperature and the final updated PV efficiency. Subsequently, the results for the CCPC-PV window with various designs are presented.

3.4.1. *Power output of original CCPC-PV window*

Fig. 21 shows that the power output of the CCPC-PV window

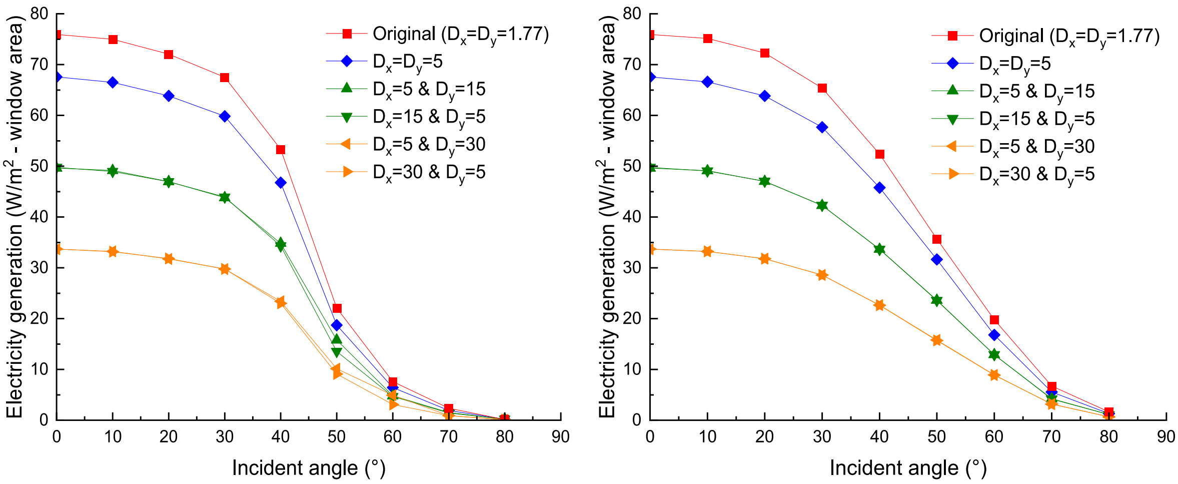

(a) 0° plane (b) 45° plane

Fig. 22. Power output of the CCPC-PV window with various designs (D_x and D_y are horizontal and vertical pitches, mm) for rays from (a) 0° plane angle and (b) 45° plane angle.

Table 5

Overall assessment for the thermal, optical, and electrical performance of the double-glazed window containing various CCPC-PV structures (D_x and D_y are horizontal and vertical pitches, mm) based on EN673 standard for calculating the U-value, and NFRC standard for calculating the SHGC, light transmittance and power output at normal incidence condition.

CCPC-PV structure	Original, D_x = D_y = 1.77	D_x = D_y = 5	D_x = 5 & D_y = 15	D_x = 5 & D_y = 30	D_x = 15 & D_y = 5	D_x = 30 & D_y = 5	No CCPC-PV
U-value (W/m^2•K)	2.575	2.566	2.657	2.573	2.706	2.575	2.805
Light transmittance (–)	0.133	0.284	0.421	0.536	0.420	0.535	0.782
SHGC (–)	0.463	0.542	0.620	0.683	0.618	0.682	0.813
Power output (W/m^2 -window area)	75.914	67.556	49.644	33.650	49.769	33.708	–

continuously decreases from 75.91 W/m^2 to approximately 0.81 W/m^2 as the incident angle increases from 0° to 80°. Because more solar energy is incident on the PV surface at higher plane angles, the system output is also larger for higher plane angles when the incident angle ranges from 40° to 80°.

3.4.2. Power output of CCPC-PV window with various designs

Fig. 22 shows the power output of the CCPC-PV window with various designs. As the pitch between adjacent CCPC optics increases, the system output decreases due to the reduced number of PV cells into the window.

4. Summary of the performance of CCPC-PV window

This section summarises previous investigations of the thermal, optical, and electrical performance of the CCPC-PV window and its various designs. The overall assessment includes the U-value (EN673 [49]), SHGC (NFRC [44]), light transmittance and power output. Among these parameters, the thermal insulation property (U-value) and light transmittance of the CCPC-PV window and its various designs have been investigated in our recent work by Li et al. (2023) [43] and the results are also listed in Table 5. For a clear traditional double-glazed window, it has been reported to experience high thermal losses in winter due to a large U-value and overheating issues in summer due to a high SHGC when installed on a south-facing façade [9,50]. Table 5 demonstrates that integrating various CCPC-PV structures between two glass panes can enhance both the thermal and energy performance of the window. This integration results in reduced U-values and SHGCs, while also generating additional power, showcasing the potential benefits of CCPC-PV windows for energy-efficient buildings. The windows with original CCPC-PV structure ($D_x = D_y = 1.77$ mm) and structure of $D_x = D_y = 5$ mm exhibit lower U-values and higher electricity generations. The limited transmission of sunlight and solar heat through the window system indicates its suitability for buildings with a large Window-to-Wall Ratio (WWR). The reduced light transmittance and SHGC values may contribute to a modest indoor luminous environment while ensuring adequate solar heat gain in winter. For building with a small WWR application, the CCPC-PV window should be designed with a larger horizontal pitch, such as 15 and 30 mm, to meet indoor illuminance requirement and ensure sufficient solar heat, while also providing enhanced thermal insulation performance and additional power output.

5. Conclusions

This study has outlined a detailed procedure for developing a comprehensive model to investigate the optical, thermal and electrical performance of complex PV window system (e.g., CCPC-PV window) using a combined CFD and ray-tracing method. The performance of the CCPC-PV window and its various designs were evaluated and compared with a similar double-glazed system. Based on the findings, the following conclusions are drawn:

1) The developed comprehensive model would be sufficient to predict the optical, thermal and electrical performance of a complex PV window system with an error of less than 4 %.
2) For original CCPC-PV window (1.77 mm-pitch), the maximum PV temperature and inside surface temperature can reach 64.73 °C and 61.58 °C, respectively, under NFRC standard. The corresponding PV efficiency in this scenario is 15.21 %.
3) Increasing the horizontal or vertical pitch between adjacent CCPC optics from 5 mm to 30 mm leads to a decrease in the average PV temperature from 58 °C to 48 °C at 0° incident angle, and a reduction in the average inside surface temperature from 54 °C to 43 °C. At the same time, the updated PV efficiency increases from 15.7 % to 16.4 %.
4) The SHGC of the CCPC-PV window is predominantly influenced by light transmittance rather than secondary heat. Consequently, windows with higher light transmittance, such as those with sparser CCPC-PV structures of $D_x = 5$ mm & $D_y = 30$ mm and $D_x = 30$ mm & $D_y = 5$ mm, exhibit the highest SHGC value (0.68) at 0° incident angle.
5) The window with a CCPC-PV structure of $D_x = 15$ mm, 30 mm & $D_y = 5$ mm provides better thermal insulation (with a smaller U-value) than those with a structure of $D_x = 5$ mm & $D_y = 15$ mm, 30 mm. These windows exhibit similar optical transmittance, SHGC value, and power output.
6) The CCPC-PV window and its various designs all exhibit advanced thermal, optical and electrical performance compared to a similarly structured double-glazed system.

The parameters obtained in this study highlight the superior optical, thermal and electrical performance of various CCPC-PV windows compared to a similarly structured double-glazed window. However, these parameters alone do not provide a complete assessment of the impact of CCPC-PV windows on building energy and daylight performance. Once installed in a building, the optical transmittance, SHGC, and system output of the window will vary with the changing solar positions throughout the year, which in turn significantly influences building energy consumption. Therefore, future research should focus on developing a building simulation model that incorporates all these dynamic properties. Such a model would offer a comprehensive evaluation of the potential energy savings and daylighting benefits that CCPC-PV windows could bring to buildings.

CRediT authorship contribution statement

Xue Li: Conceptualization, Data curation, Formal analysis, Methodology, Validation, Writing – original draft. **Yanyi Sun:** Supervision. **Xiao Liu:** Software, Validation. **Yang Ming:** Methodology, Validation. **Yupeng Wu:** Conceptualization, Funding acquisition, Methodology, Supervision, Writing – review & editing.

Declaration of competing interest

The authors declare that they have no known competing financial interests or personal relationships that could have appeared to influence the work reported in this paper.

Data availability

No data was used for the research described in the article.

Acknowledgements

This work was supported by the Faculty of Engineering, University of Nottingham and the China Scholarship Council through a joint PhD studentship awarded to Xue Li. This work was also supported by the Engineering and Physical Sciences Research Council, UK [grant number EP/S030786/1].

Appendix 1. Ray-tracing model validation

In this section, three indoor tests were carried out to validate the ray-tracing model (in **Section 2.2**) using small CPV prototypes with various devices such as solar simulator and spectrometer. The validated model was then transferred for a full-size CCPC-PV window model with dimensions of 600 mm (length) × 600 mm (height) × 28.06 mm (thickness) to investigate the solar-optical properties of the CCPC-PV window.

A1.1 Validation based on CPV attached with B270 covers

In this section, CPV prototypes with CCPC optic made of glass and topas (Polyolefin/Zeonex: COC Polymer) materials as shown in Fig. A1-1 (a) and (b) were used to conduct the ray-tracing model validation, respectively. Fig. A1-1 (c) shows the detailed configuration of these two prototypes. From the outer layer to the inter layer, it is composed of 1.1 mm-thick B270 glass cover, 0.5 mm-thick encapsulant layer (sylgard 182), 16.16 mm-thick CCPC optic, 0.5 mm-thick encapsulant layer, 0.2 mm-thick crystalline silicon solar cell (with area of 1 cm × 1 cm) [45], 1.0 mm-thick encapsulant layer and 1.1 mm-thick B270 glass cover. In addition, a T-type thermocouple was attached at the back of the PV cell to monitor the PV temperature.

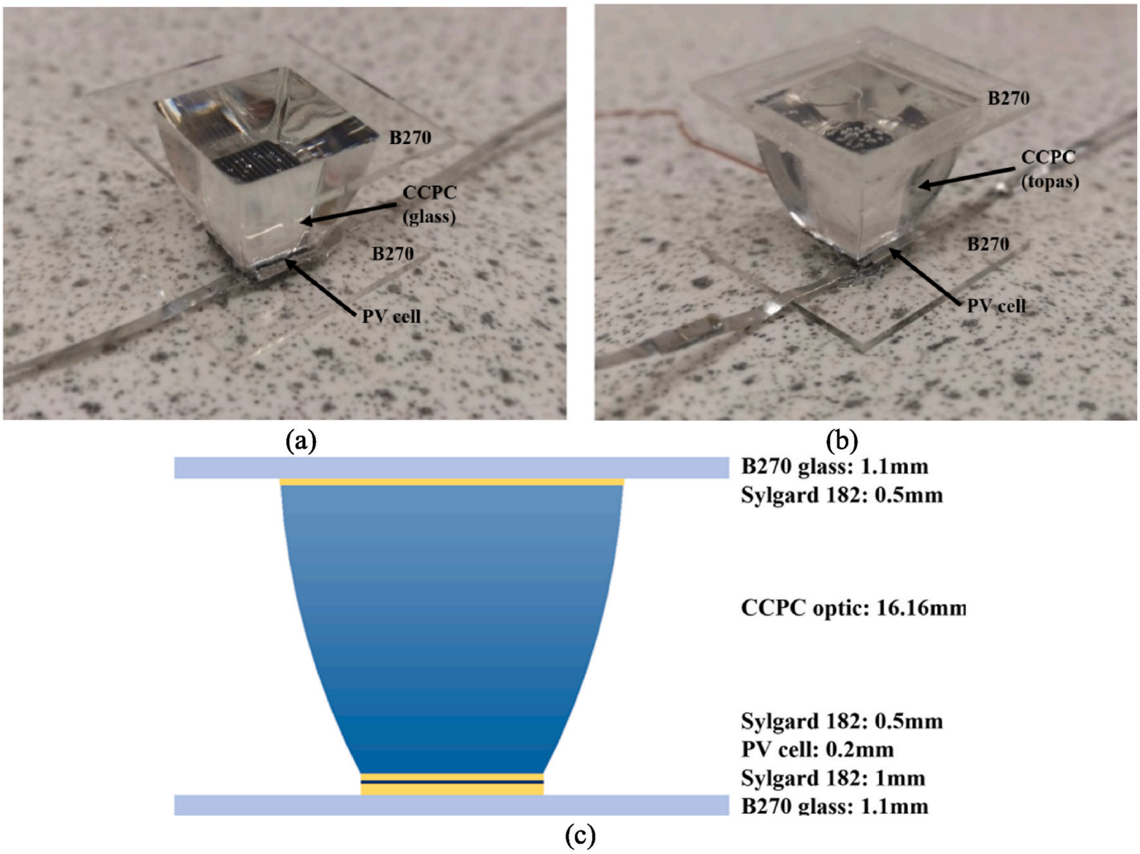

Fig. A1-1. Images of (a) glass CPV and (b) topas CPV attached with B270 covers as well as (c) its detailed configuration.

Fig. A1-2 (a) demonstrates the indoor test setup for ray-tracing model validation. The solar simulator (Oriel Sol3A Model 94063A) from Newport Corporation, which was used to provide the solar radiation with intensity of 1000 W/m^2 over a 152.4 mm × 152.4 mm area, is a class AAA category, and it is suitable for indoor test of PV modules and solar cells. The solar cell into the CPV was linked to a Keithley 2420 source meter unit via a four-wire connection method to measure its current-voltage (I–V) characteristics [51]. Besides, a fan was located behind the CPV prototype to control the cell temperature at around 25 °C, which was monitored by a T-type thermocouple connected to a datalogger DT85. The corresponding ray-tracing model used for the model validation was established as shown in Fig. A1-2 (b). The optical properties of the materials into CPV prototypes can be found in Table A1-1.

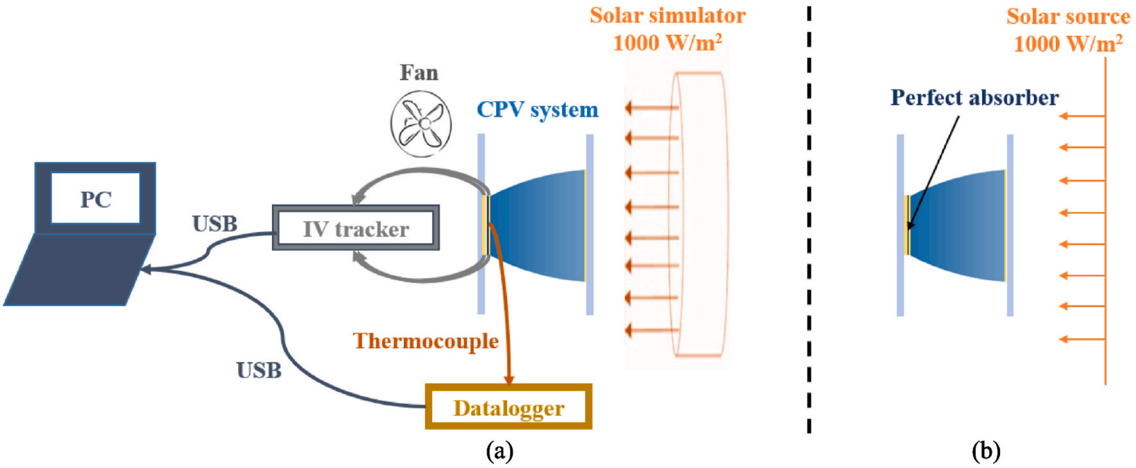

Fig. A1-2. (a) Schematic of the indoor test setup and (b) ray-tracing model.

Table A1-1
Optical properties of the materials used in the ray-tracing model validation [46,52].

Material properties	B270 glass	Topas (Polyolefin/Zeonex: COC Polymer)	Glass (Crown: CDGM –K)	Sylgard 182
Refraction index	1.523	1.53	1.523	1.41
Absorption coefficient (/mm)	0.0008	0.002	0.00007	0.01

The optical efficiency, which was defined as the ratio of the total solar energy incident on the solar cell to the total incident solar energy on the entry concentrator [53], can be calculated by Eqs. (A1-1) and (A1-2). As the ratio of the entry area of the concentrator (A_{in}) and the area of the solar cell (A_{pv}) was defined as a geometric concentration ratio (C_g) [53], the optical efficiency can also be calculated using Eqs. (A1-3). Because of the linearity property of the PV cell between the short circuit current output and the incident irradiance [54], the optical efficiency can also be estimated based on Eqs. (A1-4) [55,56].

$$\eta = \frac{Q_{pv}}{Q_{in}} \quad (A1-1)$$

$$\eta = \frac{q_{pv}A_{pv}}{q_{in}A_{in}} \quad (A1-2)$$

$$\eta = \frac{q_{pv}}{q_{in}C_g} \quad (A1-3)$$

$$\eta = \frac{I_{sc,con}}{I_{sc,nocon} \times C_g} \quad (A1-4)$$

Where, Q_{pv} is the solar energy incident on the PV surface, W. q_{pv} is the solar energy incident on the PV surface per PV area (W/m^2). Q_{in} *is* the solar energy incident on the concentrator entry surface, W. q_{in} is the solar energy incident on the concentrator entry surface per entry surface area (W/m^2). C_g is the geometric concentration ratio, 3.61 for the CCPC optic. $I_{sc,con}$ is the short circuit current of the PV cell attached with a concentrator, A. And $I_{sc,nocon}$ is the short circuit current of a bare PV cell, A.

The measurement results including the short circuit current of CPV prototypes and a bare PV cell (same electrical characteristics with those used in CPV prototypes) under the same cell temperature (25 °C) are listed in Table A1-2. Using Eqs. (A1-4), the optical efficiency was calculated as 82.0 % and 80.2 % for those attached with glass- and topas-optic, respectively. The ray-tracing results show that the incident energy on the PV surface is 3344.8 W/m^2 and 3195.2 W/m^2 for those attached with glass- and topas-optic, respectively. Using Eqs. (A1-2), the corresponding optical efficiency was calculated as 92.5 % and 88.6 %. The optical efficiency calculated based on indoor test results is 10.5 % and 8.4 % lower than that from ray-tracing simulation results. This large deviation might result from the thick encapsulant connection/optical bond between individual components causing optical loss. To be more specific, the sylgard between the front cover and optics, and that at the front and rear of solar cell might cause rays near borders to escape from the system due to similar refractive index between the CCPC optic and encapsulant. Further investigation about the heat losses is going to be discussed in **Section A1.2 and A1.3**.

Table A1-2
Optical efficiency of glass CPV and topas CPV (attached with B270 covers) calculated based on indoor test results and ray-tracing results.

PV systems	Indoor test		Ray-tracing simulation	
	Measured I_{sc}(mA)	Optical efficiency (%)	Incident irradiance on PV(W/m^2)	Optical efficiency (%)
Glass CPV with B270 cover	111.3	82.0	3344.8	92.5

(*continued on next page*)

Table A1-2 (*continued*)

PV systems	Indoor test		Ray-tracing simulation	
	Measured I_{sc}(mA)	Optical efficiency (%)	Incident irradiance on PV(W/m^2)	Optical efficiency (%)
Topas CPV with B270 cover	108.0	80.2	3195.2	88.6
Bare PV cell	37.3	–	1000	–

A1.2 Validation based on CPV.

To reduce errors leading to the above large deviation between the indoor test results and ray-tracing results, two B270 glass covers as well as the encapsulant connections between the CPV unit and two covers were removed and only a glass CPV (optics bonded to the PV) and topas CPV as shown in Fig. A1-3 were used to conduct the validation, respectively.

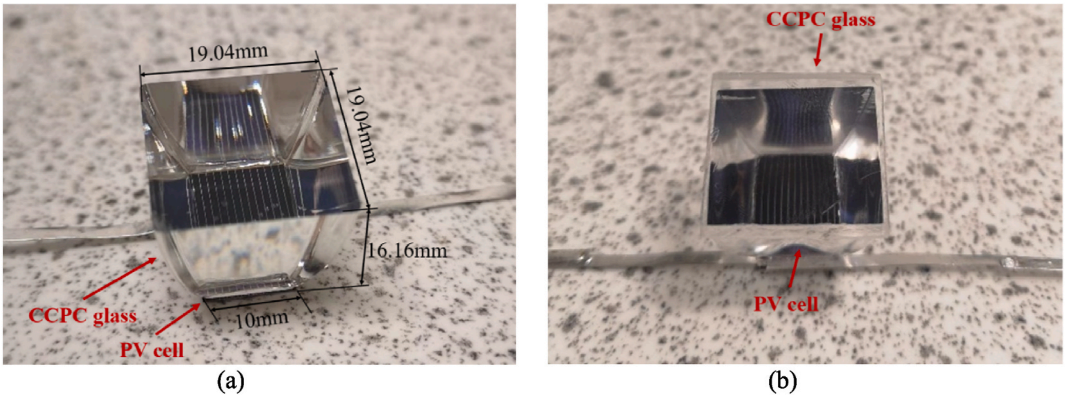

Fig. A1-3. Images of a (a) glass CPV and (b) topas CPV.

The indoor test results show a short circuit current of 116.3 mA for glass CPV and 112.3 mA for topas CPV under 1000 W/m^2 solar radiation and 25 °C PV temperature, respectively. Based on these indoor test results, the optical efficiency is determined as 86.4 % for glass CPV and 83.4 % for topas CPV, respectively. The ray-tracing simulations show that the solar energy incident on the PV surface is 3370.3 W/m^2 for glass CPV and 3216 W/m^2 for topas CPV, with optical efficiencies of 93.4 % and 89.2 %, respectively.

Table A1-3 summarises the optical efficiency obtained based on the indoor test results and ray-tracing results. The optical efficiency calculated based on the indoor test results is 7.0 % (glass CPV) and 5.8 % (topas CPV) lower than that calculated based on the ray-tracing results. Compared with the results in the last section, the deviation between indoor test results and ray-tracing results becomes smaller (from 10.5 % to 7.0 % for glass CPV and from 8.4 % to 5.8 % for topas CPV). For the ray-tracing simulation, the optical efficiency does not consider losses associated with the solar cell, such as the non-uniform energy distribution at the solar cell surface, series resistance losses, etc., which all contribute to a higher efficiency value. For the experimental test, the manufacture error, such as the bubble existing between the PV surface and CCPC optic and the inevitable spreading of the encapsulant to the border of the CCPC optic all result in a lower efficiency value. Therefore, further verification has been carried out based on a single CCPC optic discussed in **Section A1.3**.

Table A1-3
Optical efficiency of the glass CPV and topas CPV (without B270 covers) calculated based on indoor test results and ray-tracing results.

PV systems	Indoor test		Ray-tracing simulation	
	Measured I_{sc} (mA)	Optical efficiency (%)	Incident irradiance on PV (W/m^2)	Optical efficiency (%)
Glass CPV	116.3	86.4	3370.3	93.4
Topas CPV	112.3	83.4	3216	89.2
Bare PV cell	37.3	–	1000	–

A1.3 Validation based on CCPC.

Based on the above analysis, the encapsulant (Sylgard 182) connection between the CCPC optic and PV cell is inevitable to increase the optical loss. In this section, only the CCPC optic made of glass as shown in Fig. A1-4 was used to conduct the model validation. The optical flux transmitted through the CCPC optic was measured at various distances from the exit aperture of the CCPC optic and the measured results were then used to compare the data from the ray-tracing simulation.

Fig. A1-4. CCPC optic made of glass.

Fig. A1-5 (a) shows the experimental setup for model validation based one glass CCPC optic. The solar simulator was also used to provide solar radiation (1000 W/m^2 total intensity and 560 W/m^2 visible part). An irradiance probe comprised of an Ocean Optics 100-μm-core-diameter optical fibre and an Ocean Optics CC-3-UV cosine corrector was held against the rear of CCPC optic and connected to an Ocean Optics USB2000+ spectrometer (with a wavelength range of 350–1000 nm and a resolution of 0.5 nm) to detect the light (only visible part) transmitted through the CCPC optic. Then this irradiance probe was located at different distances (4, 5, 7, 10 and 15 mm) from the exit aperture of the CCPC optic to check its effect on the received optical flux. The measurement was repeated four times for each distance and the averaged value was then used to compare the ray-tracing simulation results. The corresponding ray-tracing model was established as shown in Fig. A1-5 (b). A solar source was used to provide 560 W/m^2 solar radiation (only visible part) to the entry aperture of the CCPC optic. As the light rays emitted from the solar simulator possess a maximum angle of incident of ±5° (half angle) during the indoor test, the ray-tracing simulation was also conducted at 0° and 5° incident angles to mimic the effect of this collimation angle on the validation results. A perfect absorber with 3.9 mm diameter was located at the rear of the CCPC optic to simulate the cosine corrector during the indoor test.

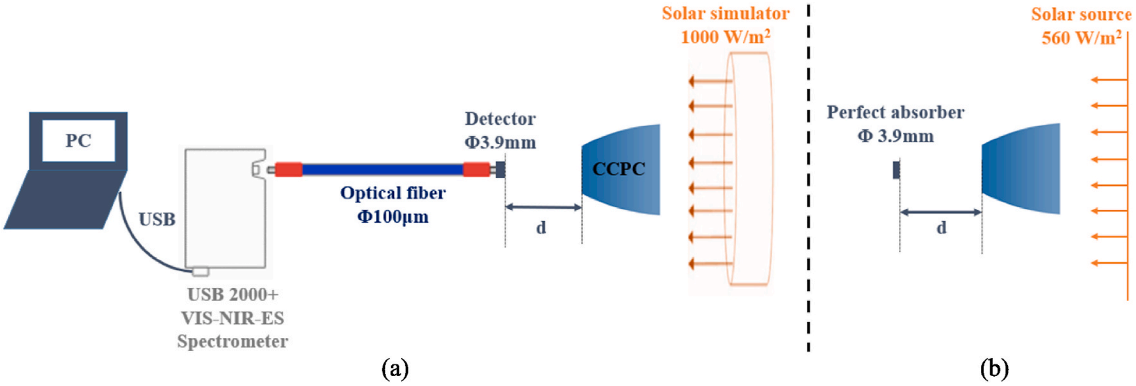

Fig. A1-5. (a) Schematic for indoor test setup and (b) corresponding ray-tracing model.

Fig. A1-6 compares the results of the indoor tests with the ray-tracing simulations for the optical flux received by the probe located at various distances. The ray-tracing simulation shows that the optical flux received by the perfect absorber increases first then decreases from 3.5 mm. It remains unchanged from 15 mm distance under 0° incident angle. This is because only the directly transmitted solar radiation can be received by the absorber when the distance between the absorber and exit aperture of CCPC optic is larger than 15 mm. The optical flux received by the absorber continuously decreases after the 15 mm distance when the incident angle is 5°. Based on the above ray-tracing results, the irradiance probe was located within 15 mm, such as 4 mm, 5 mm, 7 mm, 10 mm and 15 mm from the exit aperture of the CCPC optic during the indoor test to minimise the effect of the collimation angle on the received optical flux. The validation results show that the deviations between indoor test results and simulation results are all within 4 % across all distances.

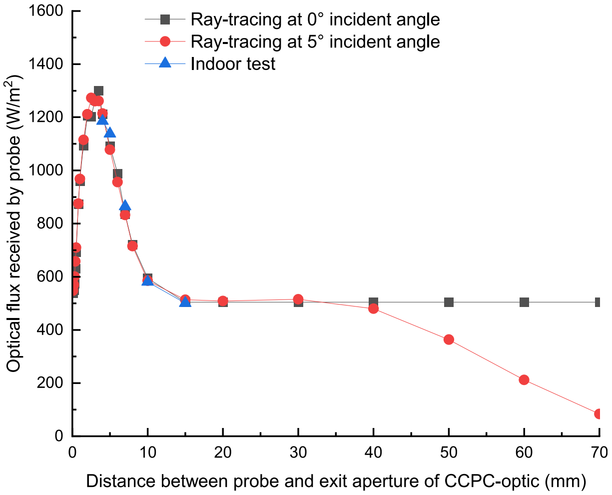

Fig. A1-6. Comparison between indoor test results and ray-tracing results.

A1.4 Summary of the ray-tracing model validation

This section summarises three validations for the ray-tracing model. For the first validation, the deviation of the optical efficiency calculated based on the indoor test results and ray-tracing results is large (10.5 % for glass CPV and 8.4 % for topas CPV). This is because the encapsulant connection between the CPV prototype and B270 covers results in large optical loss, which was not considered in the ray-tracing simulation. Through removing the B270 covers as well as the encapsulant connections between B270 covers and CPV units, this deviation can be reduced to 7.0 % for glass CPV and 5.8 % for topas CPV during the second validation. To further minimise the deviation between the indoor test and ray-tracing simulation, the PV cell as well as the encapsulant connection between the PV cell and CCPC optic were all removed and the (third) validation was conducted using a CCPC optic alone. The validation results showed that the deviations of the optical flux transmitted through the CCPC optic then received by the probe during the indoor tests and simulations are all within 4 % for all probe positions.

The glass CPV and topas CPV attached with B270 covers (Fig. A1-1) were also chosen to conduct the CFD model validation in **Appendix 2** to ensure the same boundary conditions applied as those used for the CCPC-PV window. The heat released by the PV cell into the CPV prototypes need to be input into the CFD model for model validation. However, there is a large deviation for the solar energy incident on the PV surface obtained from the indoor test and ray-tracing simulation for the CPV units attached with B270 covers. Therefore, both of the indoor test results and ray-tracing results of the solar energy incident on the PV surface were used to estimate the heat released by PV power generation and then input into the CFD model to conduct the model validation in the next section.

Appendix 2. CFD model validation and prediction of power output

Before conducting the validation for the CFD model (in **Section 2.4**), a large number of simulations for iterative convergence and mesh independence were conducted. Iterative convergence was achieved when normalized residuals were less than 10^{-3} for the continuity, and 10^{-7} for momentum and energy equations. The estimated results of the temperature field and secondary heat were calculated from the converged temperature and velocity fields. Mesh independency was achieved when the calculated window temperature and heat flux was constant as the number of nodes increased as shown in Table A2-1. There is total 457564 nodes in the CFD model and the maximum aspect ratio is around 10. Additional validation of the CFD model and power output predictions can be found in the following sections.

Table A2-1
Mesh independent results of the heat flux inward to the indoor space.

The number of nodes	15852	34776	457564	65864	92947	1097084
Average PV temperature (°C)	56.55	57.49	57.56	57.79	57.81	57.98
Average window inside surface temperature (°C)	53.02	53.55	54.13	54.17	54.16	54.33
Heat flux inward to indoor space (W/m^2)	223.46	227.54	232.03	232.28	232.20	233.52

A2.1 Indoor test.

In this section, indoor tests were conducted to further check the accuracy of the numerical simulation model. The small glass CPV and topas CPV attached with B270 covers as used for the ray-tracing model validation in **Appendix 1** (Fig. A1-1) were also employed to conduct the CFD model validation. The validated model was then transferred for a full-size CCPC-PV window model with dimensions of 600 mm (length) × 600 mm (height) × 28.06 mm (thickness) to investigate the thermal performance of the CCPC-PV window. The setup for the model validation is similar to those used for the ray-tracing model validation. However, insulation panels were used to create the adiabatic boundary conditions for the top, bottom and two side surfaces of the CPV with B270 glass covers as shown in Fig. A2-1. This setup ensures the same boundary condition as the CCPC-PV window installed into building walls. Temperature sensors and hot-wire anemometers were used to monitor the air temperature and wind speed near the test prototype. A thermocouple attached behind the PV cell was used to monitor the PV surface temperature. The fan was not used for the CFD model validation, and the PV temperature was expected to increase continuously until a steady state period. The PV temperature and power output of the CPV prototypes were retrieved during the steady state period, and the measured results were then used to compare with the CFD simulation results for model validation.

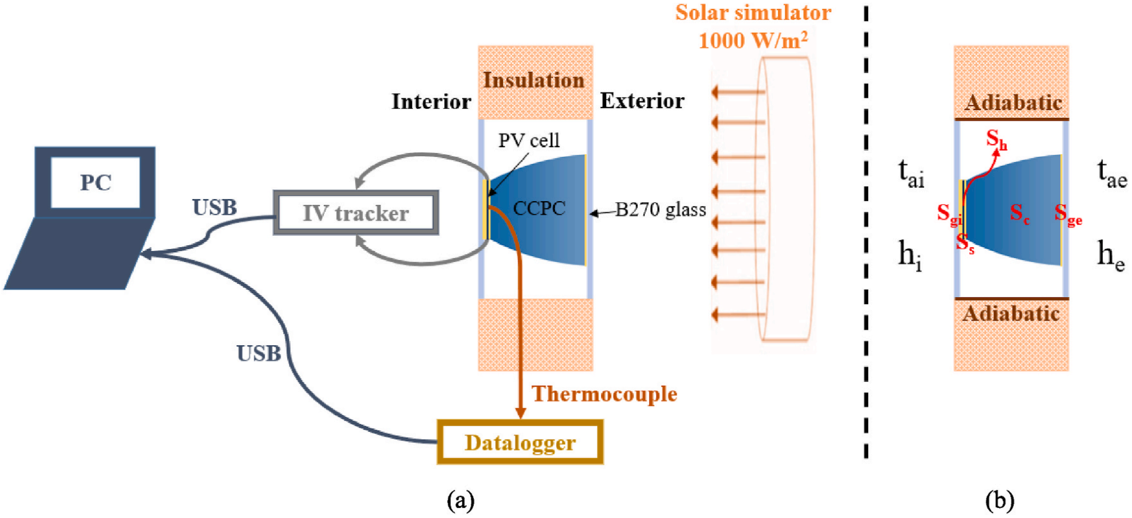

Fig. A2-1. (a) Indoor test setup for CFD model validation and (b) boundary conditions for CFD model.

A2.2 CFD simulation

Fig. A2-1(b) shows the boundary conditions obtained from the indoor test and used for the CFD simulation in a commercial CFD software package FLUENT 19.1 for model validation. Typical heat transfer boundary conditions (air temperature, t_{ai}, t_{ae} and surface heat transfer coefficient, h_i and h_e) and transformed volume heat sources (S_{gi}, S_s, S_h, S_c, and S_{ge}) were applied to the system. As mentioned in **Appendix 1** for ray-tracing model validation, there is a large deviation between the indoor test results and ray-tracing results in terms of the optical flux incident on the PV cell. Therefore, the heat released by PV power generation (S_h) was estimated based on the solar energy incident on the PV surface obtained from both of the ray-tracing simulation (q_{pv1}) and indoor test (q_{pv2}). Fig. A2-2 shows the procedure for inputting these two PV released heat sources terms (S_{h1} and S_{h2}) into the CFD model to conduct the model validation. The solar energy incident on the PV surface was simulated as 3344.8 W/m^2 (glass CPV) and 3195.2 W/m^2 (topas CPV) based on the ray-tracing results (Table A1-2). The corresponding indoor test results showed that the short circuit current of a bare PV was measured as 0.0373A under standard test condition (1000 W/m^2, AM 1.5, 25 °C) while the short circuit current of the glass CPV and topas CPV was measured as 0.111A and 0.108A under 25 °C cell temperature. Based on PV cell's linearity property between the short circuit current and incident energy on the PV surface, the incident energy on the PV surface was calculated as 2975.9 W/m^2 and 2895.4 W/m^2 for the glass CPV and topas CPV, respectively. The PV efficiency was assumed as 18 % at the beginning of the simulation. Therefore, the proportion of the PV released heat (S_{h1}) on the total solar energy incident on the outside B270 cover was calculated as 30.56 % (glass CPV) and 29.41 % (topas CPV) and the corresponding proportions were calculated as 27.19 % (glass CPV) and 26.65 % (topas CPV) for PV released heat, S_{h2}. After all these boundary conditions inputting into the CFD model, the PV efficiency was iterated based on the simulated PV temperature and the final obtained PV temperature (t_{pv1} and t_{pv2}) was compared with the experimental results (t_{pv}). Similar with the CFD model validation, the maximum power output was also calculated based on two sets of data, and the calculation results (P_1 and P_2) were also verified against the measurement result (P). The detailed information about the thermo-physical properties of the used materials as well as the boundary conditions have been listed in Table A2-2 below.

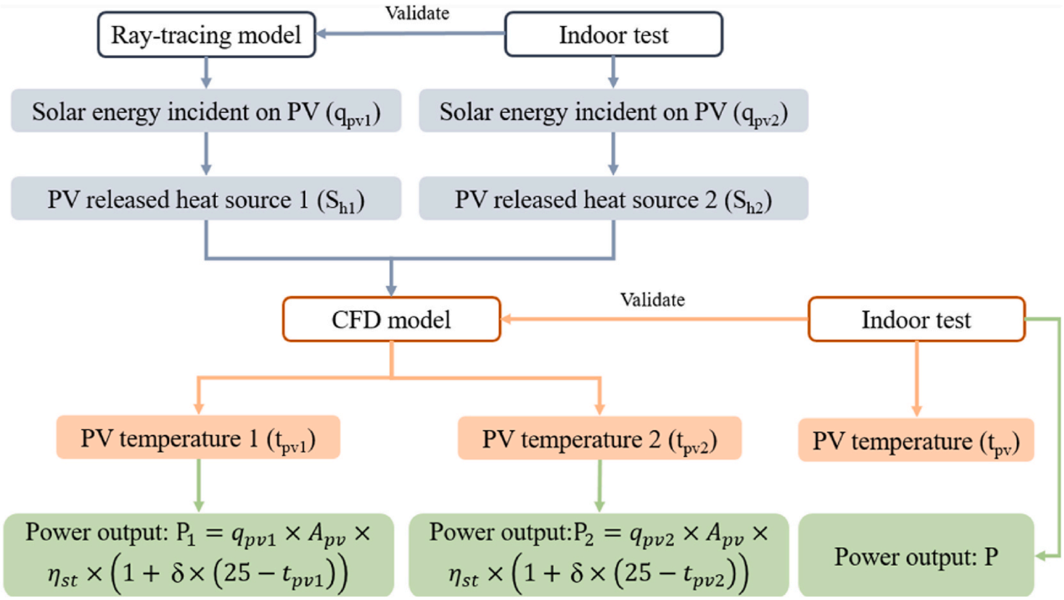

Fig. A2-2. Procedure for inputting the ray-tracing simulation results and electrical test results into the CFD model to conduct the model validation.

Table A2-2
Material properties and boundary conditions of the CFD model for model validation.

Air properties: referred in Table 4					
B270 glass properties:					
Density (kg/m^3)	Thermal conductivity (W/m· K)			Heat capacity (J/kg· K)	
2550	1			860	
PV cell properties:					
Density (kg/m^3)	Thermal conductivity (W/m· K)			Heat capacity (J/kg· K)	
2329 [45]	149 [45]			710.08	
Topas (Polyolefin/Zeonex: COC Polymer): referred in Table 4					
Glass (Crown: CDGM –K) properties:					
Density (kg/m^3)	Thermal conductivity (W/m· K)			Heat capacity (J/kg· K)	
2520	1 [46]			820	
Boundary conditions:					
➢Interior glazing	➢Exterior glazing			➢Top, bottom and two sides end	
$t_{ai} = 302.35$ K	$t_{ei} = 301.75$ K			Adiabatic	
$h_i = 7.7$ W/m^2·K	$h_e = 7.7$ W/m^2·K				
➢Heat source terms					
Components	Exterior B270 (S_{ge})	Sylgard (S_s)	CCPC (S_c)	PV cell (S_{h1}/S_{h2})	Interior B270 (S_{gi})
Glass CPV	0.11%Q_{in}	0.48%Q_{in}	0.05%Q_{in}	30.56%Q_{in}/27.19%Q_{in}	0.06%Q_{in}
Topas CPV	0.11%Q_{in}	0.47%Q_{in}	1.34%Q_{in}	29.41%Q_{in}/26.65%Q_{in}	0.06%Q_{in}

*Transmittance = 52.59 %, reflectance = 9.43 % for glass CPV prototype; Transmittance = 52.59 %, reflectance = 9.56 % for topas CPV prototype.

A2.3 Indoor test results

For the indoor test, the total testing time was approximately 4 hours to achieve the steady-state condition. The average measurements of variables (such as air temperature and PV temperature), taken from two successive 0.5-hour measuring periods after nearing stability, varied within 1 %. The air temperature and PV temperature were averaged based on the steady-state data from the last 0.5 hours. Fig. A2-3 (a) shows that after around 3 hours, the PV temperature and ambient temperature become stable. The temperature of PV cells within the glass CPV and topas CPV were averaged as 54.4 °C and 56.0 °C based on the last 0.5 hour's data as shown in Fig. A2-3 (b). The interior and exterior air temperatures were averaged as 29.2 °C and 28.6 °C. In addition to the PV temperature, three I–V curves from CPV prototypes were retrieved every 5 minute during the steady state period and the averaged data from these three curves is shown in Fig. A2-4. The maximum power output was found as 0.049 W and 0.046 W for the glass CPV and topas CPV, respectively.

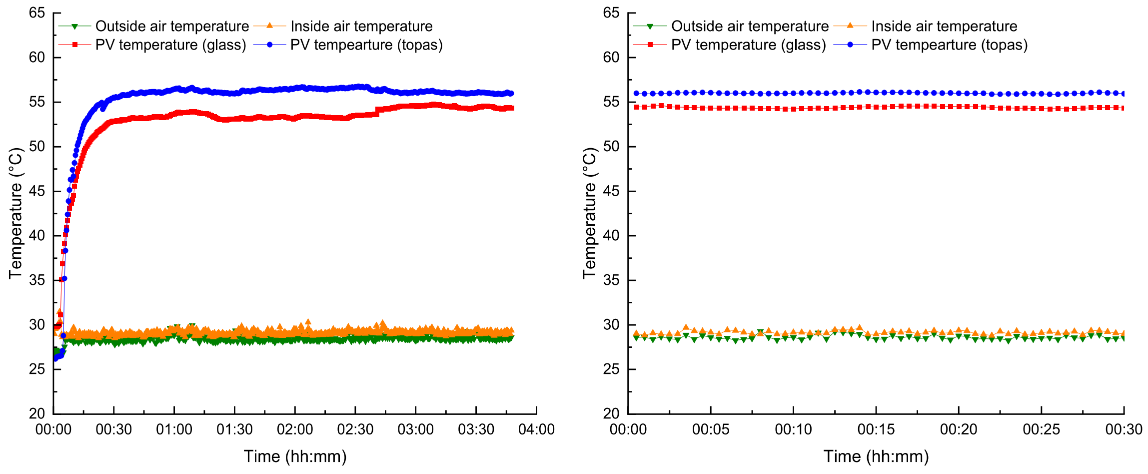

(a) (b)

Fig. A2-3. Cell temperature and ambient temperature for (a) around 4 h' light exposure and (b) last half an hour's light exposure.

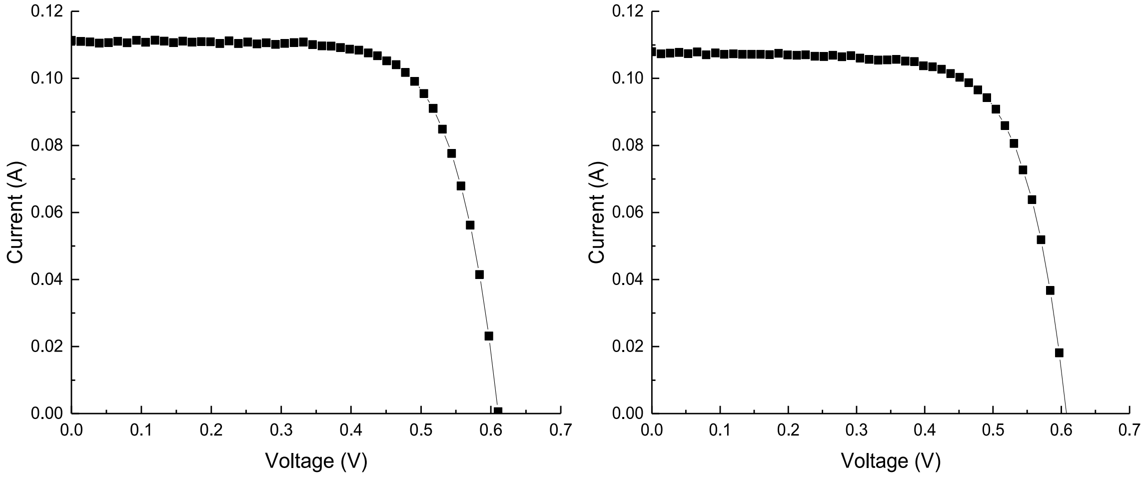

(a)

(b)

Fig. A2-4. I–V curves retrieved from the PV cell into the (a) glass CPV prototype and (b) topas CPV prototype during the steady state period.

A2.4 CFD simulation results

Fig. A2-5 shows the temperature profile of the glass CPV and topas CPV when the PV released heat calculated from ray-tracing results (S_{h1}) was input into the CFD model. The averaged PV temperatures for glass CPV and topas CPV were simulated as 58.9 °C and 64.4 °C, respectively. Fig. A2-6 shows the temperature profile when the PV released heat obtained from experimental results (S_{h2}) was input into the CFD model. The averaged PV temperatures were calculated as 55.61 °C and 61.03 °C for glass CPV and topas CPV, respectively.

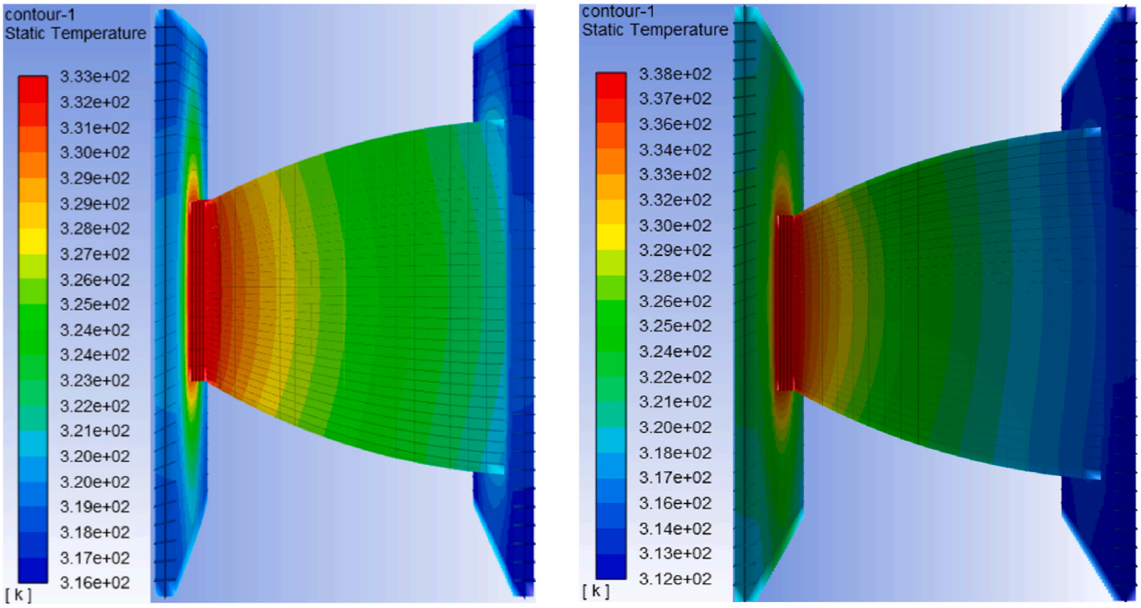

(a)

(b)

Fig. A2-5. Temperature profile of the (a) glass CPV and (b) topas CPV for the PV released heat (S_{h1}) inputting into the CFD model.

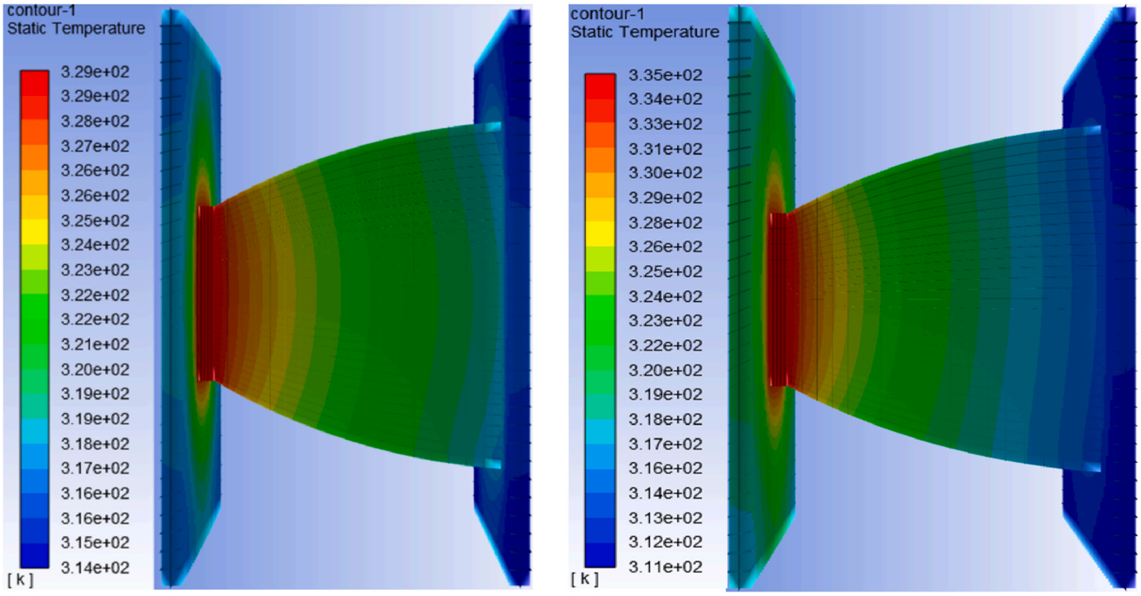

(a) (b)

Fig. A2-6. Temperature profile of the (a) glass CPV and (b) topas CPV for the PV released heat (S_{h2}) inputting into the CFD model.

Table A2-3 compares the PV temperature obtained from indoor tests and CFD simulations. There is a large deviation (8.3 % for glass CPV and 15 % for topas CPV) when the PV released heat (S_{h1}) was input into the CFD model. This is because a large amount of optical loss into the CPV prototype was not considered during the ray-tracing simulation. When this energy term was estimated based on the short circuit current of a bare PV cell and the CPV under same cell temperature (S_{h2}), there is only 2.2 % deviation between the indoor test and CFD simulation for the glass CPV. The corresponding deviation for the topas CPV is 8.9 %. The PV temperature from the indoor test (56.0 °C) is lower than that from the CFD simulation (61.0 °C). This large deviation is mainly because of the bubble generated between the PV cell and interior B270 cover, which displaces the thermocouple toward the edge area of the PV cell.

Table A2-3
PV temperature of the glass CPV and topas CPV (attached with B270 covers).

CPV systems	Indoor test	CFD simulation	
		t_{pv1} (δ)	t_{pv2} (δ)
Glass CPV	54.4 °C	58.9 °C (8.3 %)	55.6 °C (2.2 %)
Topas CPV	56.0 °C	64.4 °C (15.0 %)	61.0 °C (8.9 %)

'δ' is the deviation between CFD simulation results and indoor test results.

Based on the solar energy incident on the PV surface (Q_{pv}) obtained during the ray-tracing model validation in Appendix 1 and PV temperature (t_{pv}) obtained in this section as well as the electrical test results of the PV efficiency at standard test condition (η_{st}) and temperature coefficient (α) in Section 2.3, the maximum power output of the PV cell can be calculated using Eq. (A2-1)and Eq. (A2-2). Considering the large optical loss into the CPV prototypes, the maximum power output was also calculated based on two sets of data. For the first set, the solar energy incident on the PV surface (q_{pv1}) was estimated from ray-tracing simulation results while the PV temperature (t_{pv1}) was obtained based on the CFD modelling when the PV released heat, S_{h1}, was input into the CFD model. In the second set, the solar energy incident on the PV surface (q_{pv2}) was estimated from the measured short circuit current while the PV temperature (t_{pv2}) was obtained based on the CFD modelling when the PV released heat, S_{h2}, was input into the CFD model. Based on these two sets of data, the maximum power output can be calculated to verify the measured results in Fig. A2-4.

$$P_1 = q_{pv1} \times A_{pv} \times \eta_{st} \times \left(1 + \alpha \times \left(25 - t_{pv1}\right)\right) \quad (A2-1)$$

$$P_2 = q_{pv2} \times A_{pv} \times \eta_{st} \times \left(1 + \alpha \times \left(25 - t_{pv2}\right)\right) \quad (A2-2)$$

Where, P_1 and P_2 are the maximum power produced by the PV cell, W. q_{pv1} and q_{pv2} are the solar energy incident on the PV cell, W/m^2. A_{pv} is the cell area, m^2. η_{st} is the PV conversion efficiency under standard test condition. α is the temperature coefficient,/°C. t_{pv1} and t_{pv2} are the PV temperature, .

Based on Eq. (A2-1), the maximum power output was calculated as 0.057 W and 0.049 W for glass CPV and topas CPV, respectively. It was calculated as 0.050 W and 0.047 W, respectively, based on Eqs. (A2-2). Table A2-4 compares the power output of the CPV prototypes obtained from indoor tests and calculations. There is a large deviation (16.3 % for glass CPV and 6.5 % for topas CPV) between the indoor test result and calculation result based on Eq. (A2-1). This is because a large amount of optical loss into the CPV prototypes (with B270 glass covers) was not considered during the ray-tracing simulation, which leads to much higher estimation of incident energy on the PV surface. When the power output was calculated based on Eqs. (A2-2), there is only 2.0 % (glass CPV) and 2.2 % (topas CPV) deviation between the indoor test result and calculation result.

Table A2-4
Power output of the glass CPV and topas CPV (attached with B270 covers).

CPV systems	Indoor test	CFD simulation	
		P_1 (δ)	P_2 (δ)
CPV (glass)	0.049 W	0.057 W (16.3 %)	0.050 W (2.0 %)
CPV (topas)	0.046 W	0.049 W (6.5 %)	0.047 W (2.2 %)

‘δ’ is the deviation between indoor test and calculation based on Eq. (A2-1)and Eqs. (A2-2).

A2.5 Summary of the CFD model validation

This section summarises the validations of the CFD model for the thermal characterisation of the CCPC-PV window, based on indoor tests with small CPV prototypes. The PV temperature and power output of the CPV prototypes were measured during the steady state period and the measured results were compared with the corresponding combined CFD and ray-tracing results. The validation results showed that there was a large deviation of PV temperature (more than 10 %) when the PV released heat estimated through ray-tracing simulation results was input into the CFD model because of the optical loss into the CPV prototype is not included in the ray-tracing simulation. When this energy term was estimated based on the experimental results, the deviation becomes smaller (less than 3 %). Similar for the power output, there was a large deviation (more than 15 %) between the indoor test result and calculation result based on the combined CFD and ray-tracing method when the solar energy incident on the PV surface was estimated through ray-tracing simulations. When this energy term was estimated through experimental data, this deviation was only 2.0 % for glass CPV and 2.2 % topas CPV.

Based on the above analysis, it can be seen that the main reason for causing the deviation of the PV temperature and power output between indoor test results and CFD combined ray-tracing results is because of the optical loss existing into the thick encapsulant connection in the CPV prototypes. This thick encapsulant connection results from the presence of the thermocouple at the back of the PV cell as well as the inexperience of making CPV units. None of these issues exists for the professionally made CCPC-PV window. Therefore, the established numerical simulation model can be used for thermal characterisation of the CCPC-PV window with dimensions of 600 mm (length) × 600 mm (height) × 28.06 mm (thickness).

Appendix 3. Light transmittance of the CCPC-PV windows

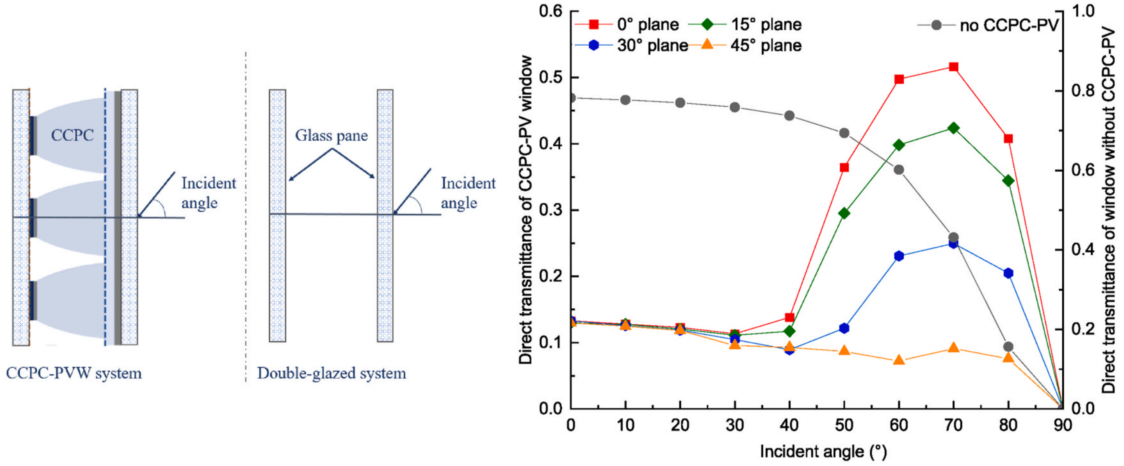

(a) (b)

Fig. A3-1. (a) Incident angle (θ) of the window and (b) light transmittance of the original CCPC-PV window and double-glazed window.

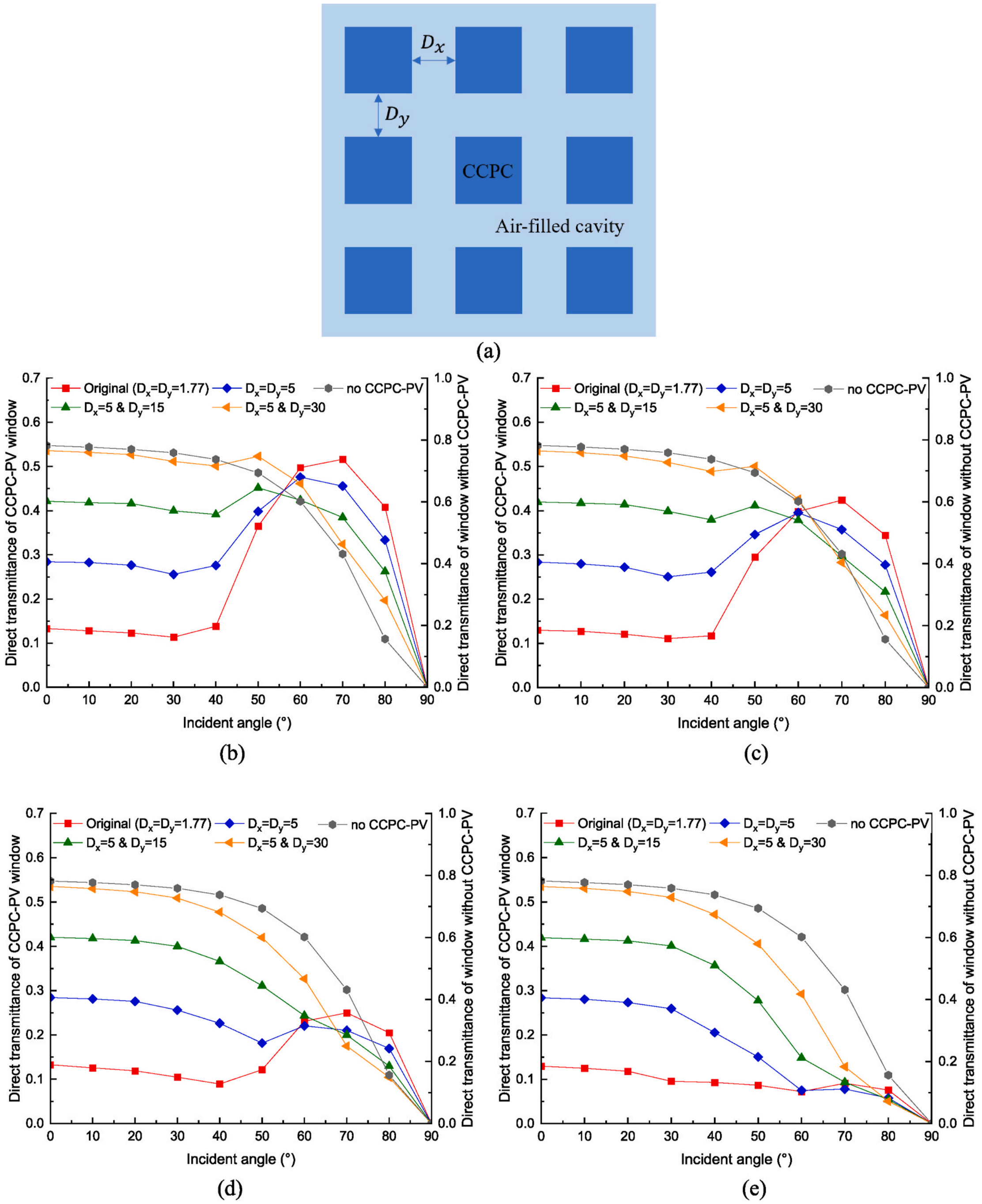

(a)

(b)

(c)

(d)

(e)

Fig. A3-2. (a) Horizontal pitch (D_x, mm) and vertical pitch (D_y, mm) between adjacent CCPC optics, light transmittance of the double-glazed window containing various CCPC-PV structures for rays from (b) 0°, (c) 15°, (d) 30° and (e) 45° planes.

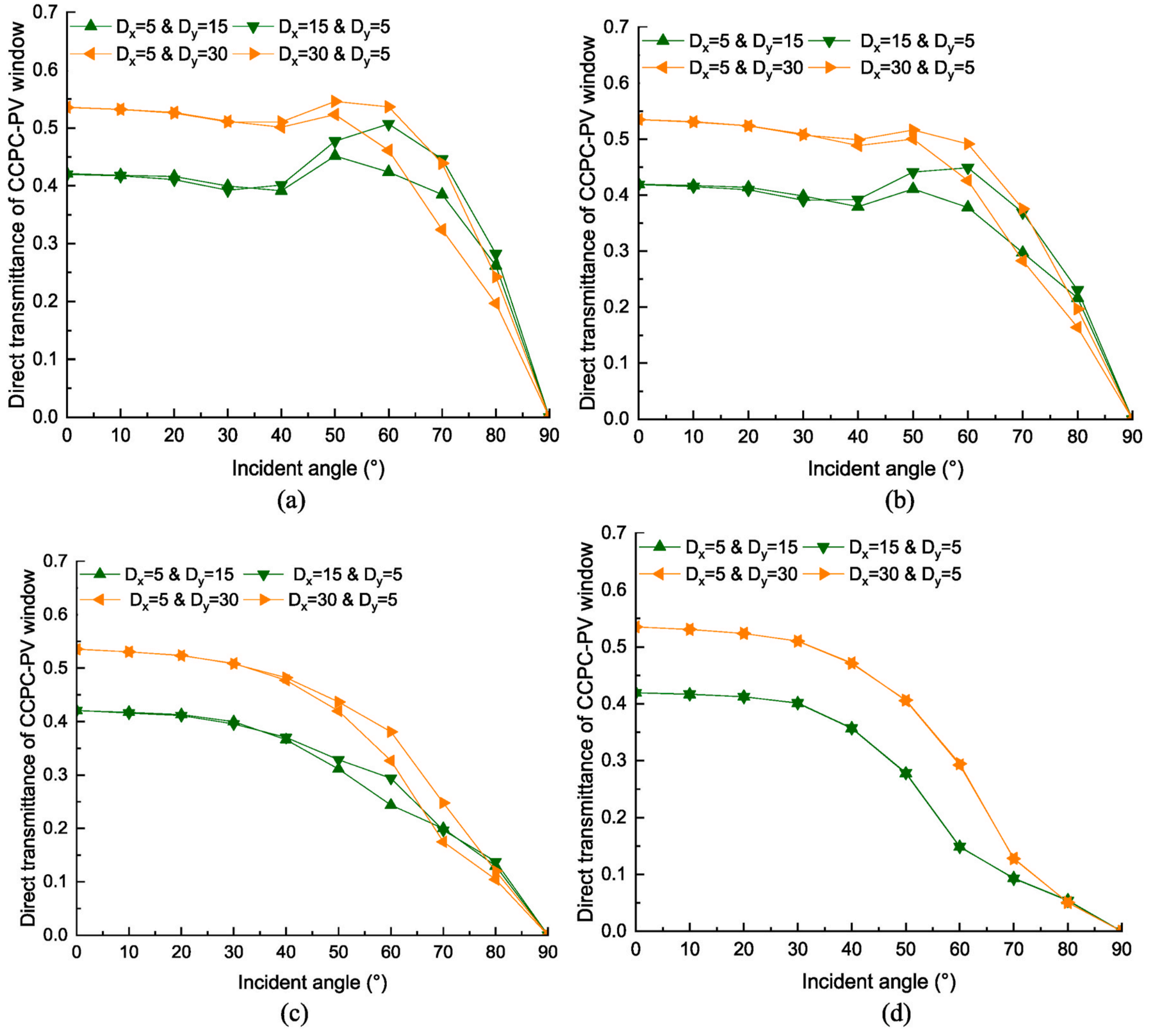

Fig. A3-3. Comparison of the light transmittance of the double-glazed window containing a CCPC-PV structure of $D_x = 5$ & $D_y = 15$, 30 and $D_x = 15$, 30 & $D_y = 5$ for rays from (a) 0°, (b) 15°, (c) 30°, and (d) 45° planes (D_x and D_y are horizontal and vertical pitches, mm).

References

[1] Gosselin L, Dussault J-M. Correlations for glazing properties and representation of glazing types with continuous variables for daylight and energy simulations. Sol Energy 2017;141:159–65.

[2] Field E, Ghosh A. Energy assessment of advanced and switchable windows for less energy-hungry buildings in the UK. Energy 2023;283:128999.

[3] Harmathy N, Magyar Z, Folić R. Multi-criterion optimization of building envelope in the function of indoor illumination quality towards overall energy performance improvement. Energy 2016;114:302–17.

[4] Xu Y, et al. A multi-objective optimization method based on an adaptive meta-model for classroom design with smart electrochromic windows. Energy 2022;243:122777.

[5] Aguilar-Santana JL, et al. Review on window-glazing technologies and future prospects. Int J Low Carbon Technol 2020;15(1):112–20.

[6] Pu J, Shen C, Lu L. Investigating the annual energy-saving and energy-output behaviors of a novel liquid-flow window with spectral regulation of ATO nanofluids. Energy; 2023, 129111.

[7] Ghosh A. Investigation of vacuum-integrated switchable polymer dispersed liquid crystal glazing for smart window application for less energy-hungry building. Energy 2023;265:126396.

[8] Mesloub A, et al. Assessment of the overall energy performance of an SPD smart window in a hot desert climate. Energy 2022;252:124073.

[9] Tällberg R, et al. Comparison of the energy saving potential of adaptive and controllable smart windows: a state-of-the-art review and simulation studies of thermochromic, photochromic and electrochromic technologies. Sol Energy Mater Sol Cell 2019;200:109828.

[10] Akram MW, et al. Global technological advancement and challenges of glazed window, facade system and vertical greenery-based energy savings in buildings: a comprehensive review. Energy and Built Environment; 2021.

[11] Sun Y, et al. Thermal evaluation of a double glazing façade system with integrated Parallel Slat Transparent Insulation Material (PS-TIM). Build Environ 2016;105:69–81.

[12] Sun Y, Wu Y, Wilson R. Analysis of the daylight performance of a glazing system with parallel slat transparent insulation material (PS-TIM). Energy Build 2017;139:616–33.

[13] Khaled Mohammad A, Ghosh A. Exploring energy consumption for less energy-hungry building in UK using advanced aerogel window. Sol Energy 2023;253:389–400.

[14] Hassani AR, et al. Evaluation of the solar heat gain coefficient of innovative aerogel glazing systems: experimental campaigns and numerical results. J Build Eng 2022;62:105354.

[15] Wang M, et al. Comparison of energy performance between PV double skin facades and PV insulating glass units. Appl Energy 2017;194:148–60.

[16] Abolghasemi Moghaddam S, Simões N, Gameiro da Silva M. Review of the experimental methods for evaluation of windows' solar heat gain coefficient: from standardized tests to new possibilities. Build Environ 2023;242:110527.

[17] Kuhn TE. Calorimetric determination of the solar heat gain coefficient g with steady-state laboratory measurements. Energy Build 2014;84:388–402.

[18] Marinoski DL, et al. Improvement of a measurement system for solar heat gain through fenestrations. Energy Build 2007;39(4):478–87.

[19] Peng J, Lu L, Yang H. An experimental study of the thermal performance of a novel photovoltaic double-skin facade in Hong Kong. Sol Energy 2013;97:293–304.

[20] Peng J, et al. Comparative study of the thermal and power performances of a semi-transparent photovoltaic façade under different ventilation modes. Appl Energy 2015;138:572–83.

[21] Nie Z, et al. Adaptive Façades Strategy: an architect-friendly computational approach based on co-simulation and white-box models for the early design stage. Energy Build 2023;296:113320.

[22] Wang C, et al. Design and performance investigation of a novel double-skin ventilated window integrated with air-purifying blind. Energy 2022;254:124476.

[23] Martín-Chivelet N, et al. Building-Integrated Photovoltaic (BIPV) products and systems: a review of energy-related behavior. Energy Build 2022;262:111998.

[24] Peng J, et al. Numerical investigation of the energy saving potential of a semi-transparent photovoltaic double-skin facade in a cool-summer Mediterranean climate. Appl Energy 2016;165:345–56.

[25] ISO. Thermal performance of windows, doors and shading devices–Detailed calculations. 2003, 15099.

[26] Din EN. Glas im Bauwesen–Bestimmung der lichttechnischen und strahlungsphysikalischen Kenngrößen von Verglasungen. Deutsche Fassung EN 2011:410. 410: 2011-04.

[27] Baenas T, Machado M. On the analytical calculation of the solar heat gain coefficient of a BIPV module. Energy Build 2017;151:146–56.

[28] Window 7. WINDOW Technical Documentation; 2018.

[29] Chen F, et al. Solar heat gain coefficient measurement of semi-transparent photovoltaic modules with indoor calorimetric hot box and solar simulator. Energy Build 2012;53:74–84.

[30] Villalba A, et al. Hot-cool box calorimetric determination of the solar heat gain coefficient and the U-value of internal shading devices. Energy Efficiency 2017;10 (6):1553–71.

[31] ISO. Thermal performance of windows and doors—determination of solar heat gain coefficient using solar simulator. 2017, 19467.

[32] Simmler H, Binder B. Experimental and numerical determination of the total solar energy transmittance of glazing with Venetian blind shading. Build Environ 2008; 43(2):197–204.

[33] Kersken M. Method for the climate-independent determination of the solar heat gain coefficient (SHGC; g-value) of transparent façade and membrane constructions from in situ measurements. Energy Build 2021;239:110866.

[34] Craig KJ, et al. Using CFD and ray tracing to estimate the heat losses of a tubular cavity dish receiver for different inclination angles. Sol Energy 2020;211:1137–58.

[35] Craig KJ, Marsberg J, Meyer JP. Combining ray tracing and CFD in the thermal analysis of a parabolic dish tubular cavity receiver. AIP Conf Proc 2016;1734(1): 030009.

[36] Li Z, et al. Study on the radiation flux and temperature distributions of the concentrator–receiver system in a solar dish/Stirling power facility. Appl Therm Eng 2011;31(10):1780–9.

[37] Wang W, et al. Conjugate heat transfer analysis of an impinging receiver design for a dish-Brayton system. Sol Energy 2015;119:298–309.

[38] Zhang Y, et al. Combined optics and heat transfer numerical model of a solar conical receiver with built-in helical pipe. Energy 2020;193:116775.

[39] Daabo AM, et al. Numerical investigation of pitch value on thermal performance of solar receiver for solar powered Brayton cycle application. Energy 2017;119: 523–39.

[40] Du S, et al. Pore-scale numerical simulation of fully coupled heat transfer process in porous volumetric solar receiver. Energy 2017;140:1267–75.

[41] Demanega Iea. CFD and ray tracing to evaluate the thermal performance of complex fenestration systems. 2018.

[42] Baig H, et al. Numerical modelling and experimental validation of a low concentrating photovoltaic system. Sol Energy Mater Sol Cell 2013;113:201–19.

[43] Li X, et al. Comprehensive investigation of a building integrated crossed compound parabolic concentrator photovoltaic window system: thermal, optical and electrical performance. Renew. Energy 2024;223:119791.

[44] NFRC 200-2014. Procedure for determining fenestration product solar heat gain Coefficient and visible Transmittance at normal incidence. 2014.

[45] Baig H, et al. Performance analysis of a dielectric based 3D building integrated concentrating photovoltaic system. Sol Energy 2014;103:525–40.

[46] Shanks K, et al. An experimental analysis of the optical, thermal and power to weight performance of plastic and glass optics with AR coatings for embedded CPV windows. Sol Energy Mater Sol Cell 2019;200:110027.

[47] Ren X-H, et al. Thermal driven natural convective flows inside the solar chimney flush-mounted with discrete heating sources: Reversal and cooperative flow dynamics. Renew Energy 2019;138:354–67.

[48] Rath S, Dash SK. Numerical study of laminar and turbulent natural convection from a stack of solid horizontal cylinders. Int J Therm Sci 2020;148:106147.

[49] BS EN 673:2011. Glass in building. Determination of thermal transmittance (U value). Calculation method. British Standards Institute; 2011.

[50] Qiu C, Yang H. Daylighting and overall energy performance of a novel semi-transparent photovoltaic vacuum glazing in different climate zones. Appl Energy 2020;276:115414.

[51] Liu X, Wu Y. Experimental characterisation of a smart glazing with tuneable transparency, light scattering ability and electricity generation function. Appl Energy 2021;303:117521.

[52] Sun Y, et al. Thermal evaluation of a double glazing façade system with integrated Parallel Slat Transparent Insulation Material (PS-TIM) 2016;105.

[53] Wu Y, et al. Smart solar concentrators for building integrated photovoltaic façades. Sol Energy 2016;133:111–8.

[54] Müllejans H, Salis E. Linearity of photovoltaic devices: quantitative assessment with N-lamp method. Meas Sci Technol 2019;30(6):065008.

[55] Ferrer-Rodríguez JP, et al. Development, indoor characterisation and comparison to optical modelling of four Fresnel-based high-CPV units equipped with refractive secondary optics. Sol Energy Mater Sol Cell 2018;186:273–83.

[56] Mammo ED, Sellami N, Mallick TK. Performance analysis of a reflective 3D crossed compound parabolic concentrating photovoltaic system for building façade integration. Prog Photovoltaics Res Appl 2013;21(5):1095–103.